2007

Corrosion assessment of mechanically formed aluminized steel

Mersedeh Akhoondan
University of South Florida

Corrosion Assessment of Mechanically Formed Aluminized Steel

by

Mersedeh Akhoondan

A thesis submitted in partial fulfillment
of the requirements for the degree of
Master of Science in Civil Engineering
Department of Civil & Environmental Engineering
College of Engineering
University of South Florida

Major Professor: Alberto Sagüés, Ph.D.
Noreen Poor, Ph.D.
Rajan Sen, Ph.D.

Date of Approval:
November 1, 2007

Keywords: Spiral Ribbed Pipes, Corrugated, Microfissures, Scale-Forming Waters, Electrochemical Behavior

Dedication

This work is dedicated to:

My mother, Taraneh Bahary

Your encouragement and comforting words are a tonic for my soul.

My father, Ali Akhoondan

Your unconditional love and sacrifices continue to enrich my life.

My sister, Mandana

Your friendship is a treasure beyond compare.

Also, my Uncle Majid and the rest of my family who always supported me and provided me with the means to finish this project.

Acknowledgments

First, I would like to sincerely appreciate Dr. Alberto Sagüés, my mentor and supervisor for his sage advice, insightful criticism, and patient encouragement.

Also, I appreciate the help and guidance of Dr. Leonardo Caseres, the pioneer in this investigation.

I gratefully acknowledge support from the Florida Department of Transportation and the Federal Highway Administration in funding this research.

The opinions, findings, and conclusions expressed here are those of the author and not necessarily those of the supporting agency.

Table of Contents

List of Tables

List of Figures

Corrosion Assessment of Mechanically Formed Aluminized Steel

Mersedeh Akhoondan

ABSTRACT

Ribbed steel pipes made of Type 2 aluminized steel are commonly used for culvert pipes for highway drainage. Typically aluminized steel pipes have shown good durability and are expected to have long service life, e.g. 75 years; also, they are used in a wide variety of soil and water conditions. However, early corrosion of aluminized steel pipes has been recently observed in some inland locations. Initial observations showed severe corrosion in forms of pits, both along the ribs and at the nearby flat portions of the pipes. It is critical to determine the cause of early deterioration and establish methods of durability prediction. The possibility of unusual environmental conditions is being investigated elsewhere, but this research focuses on possible mechanical factors aggravating corrosion, since it is prevalent near pipe rib deformations. While forming the rib bends in the pipe, the outer bend surface is exposed to extreme tensile stresses which would cause small coating cracks (microfissures) exposing base metal. Those may lead to early corrosion as galvanic protection from the surrounding aluminum may not be sufficient under certain environments.

Electrochemical impedance spectroscopy was used to measure corrosion rate of both formed and flat aluminized steel samples in simulated natural waters. Initial findings

show that specimens formed by spherical indentation were susceptible to early corrosion development in moderately aggressive simulated natural water, but not in a more benign, precipitating simulated natural water solution.

Chapter One

Introduction

Aluminum and aluminum alloys represent an important category of materials due to their high technological value and wide range of industrial applications. Aluminum is also used as metallic coating for steel. It has been shown that aluminized steel is superior over galvanized steel sheets in corrosion resistance (Cerlanek and Powers, 1933) with up to 6 times longer service life. In galvanized steel the zinc coating is subject to continuous corrosion to provide protection, while in aluminized steel corrosion resistance is provided mainly by a stable thin film of aluminum oxide. If this film is damaged or removed by abrasion, another layer of oxide is expected to form instantly to avoid further corrosion. Two types of aluminized steel are produced: Type 1 which have an aluminum coating with addition of 10% silicon to provide corrosion as well as heat resistance. Aluminized Type 1 is commonly used in high temperature automobile industry applications (muffler systems and heat exchangers).Type 2, however, has aluminum coating and its typically applications are commercial roofing and culvert pipes.

1.1 Background on Aluminized Steel Type 2

Aluminized steel Type 2 is produced as a steel sheet, hot-dip coated on both sides with commercially pure aluminum (ASTM A929 and ASSHTO M274), which provides corrosion protection through low corrosion rate of the aluminum when the aluminum is in passive condition, and also may confer galvanic protection to the exposed underlying

steel under certain circumstances (Kimoto, 1999). For that reason, aluminized steel Type 2 is increasingly used for metallic drainage components in contact with natural waters. However, corrosion is an important durability limitation factor in these components, which are often designed for very long service life (e.g. 75 yrs) (Cerlanek and Poweres, 1993).

Microscopic examination of aluminized steel Type 2 in cross section shows a nearly pearlite-free ferrite low carbon steel substrate with regular grains, a partly columnar brittle inner alloy layer ~15 μm thick, and a softer outer aluminum-rich layer ~30 μm thick. The inner alloy layer, commonly of composition Fe_2Al_5 (An, Lui and Sun, 2001), (Li et al., 2003) is an essential ingredient of the coating protection system, supplementing the outer aluminum-rich layer and possibly providing a second line of defense against corrosion. The composition of the outer layer is predominantly nearly pure aluminum with Fe-rich intermetallic precipitates (6-11 wt% Fe) (Caseres and Sagüés, 2005). During manufacturing and/or handling of the final material, discontinuities in the aluminized coating can extend to the substrate steel, creating coating breaks. Those coating breaks exposing the steel base may result in the formation of galvanic macrocells. However, if the environment is mild as those commonly found in Florida inland waters, sacrificial protection to the exposed underlying steel may not be sufficient to prevent early corrosion as visually noted by the growth of rust projections at the aluminized coating breaks.

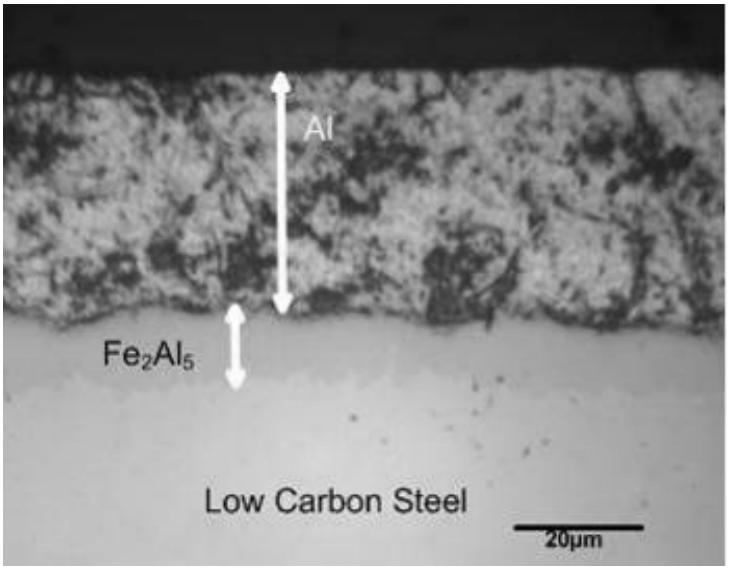

Figure 1-1. Aluminized Steel Type 2 Microstructure. (The outer layer contains additional small amounts of aluminum-iron intermetallic precipitates).

1.2 Spiral Ribbed Pipe-Forming Process

The ASTM 760 specification applies to the fabrication of ribbed pipes. The general process used to form the spiral ribs are as follows: The stock aluminized sheet is rolled over a series of press dies while it is lubricated with a soapy solution in order to decrease friction. Such construction creates open type ribs. Interlocking folds are formed in the opposite side of the sheet. As the pipe is rolled into the spiral, the interlocking fold connects with a corresponding fold on the rib. These formed, not-welded interlocks are called lock-seams and join the segments of spiral pipes.

Figure 1-2. Spiral Rib Pipe Manufacturing Process (Dies Used to Form Rib (Left), Forming Spiral Pipe (Right)). [Photograph by the Author]

During the fabrication of pipes, minor scratches and surface blemishes due to the rolling process and handling of the pipes are normal. As shown in Figure 1-3, aluminized stock rolls over against other metal components during the forming process, and signs of minor scratching are readily observed.

Figure 1-3. Minor Scratches During Fabrication Spiral Rib Pipe. [Photograph by the Author].

1.3 Durability of Corrugated Culvert Pipe

1.3.1 Field Investigations

Aluminized steel is commonly used for metallic culvert pipes. This type of pipes is expected to have a long range service life from decades to beyond. The recommended condition for application of these pipes is pH rage of 5-9 and soil resistivity above 1500 ohm/cm (Kimoto, 1999). The minimum gage thickness for steel culverts and storm drains should be no less than 16-gage (Bednar, 1989). The gage thickness required for all performance modes should be determined for each installation based on soil type, height of fill, and compaction of that soil (Cerlanek and Powers, 1993). The FDOT culvert pipe durability and materials selections guidelines (Cerlanek and Powers, 1993) project very long service life for aluminized culvert pipe under those conditions. Earlier field investigations (Bednar, 1989) also indicate good prognosis for extended service life. However, recent field inspections conducted by FDOT on four-year old spiral rib aluminized steel Type 2 culvert pipes exposed to Florida inland waters have shown unexpected severe corrosion damage of aluminized pipe in the form of pits and generalized corrosion at the pipe ribs (where material forming was more intense) and less so but still noticeable corrosion damage at the nearby flat portions of the pipe. The cause of that deterioration is under investigation, of which the present work is a part.

Figure 1-4. Corroded Pipe from the Curlew Rd. Site, Pinellas County, Fla. (2007) [Photograph by the Author].

1.4 Review of Relevant Information on Characteristics and Corrosion Performance of Aluminized Steel.

1.4.1 The Morphology of Intermetallic Layer in Hot-dip Aluminized Steels

An important factor which directly affects the mechanical characteristics of aluminized steel is the thickness of intermetallic layer, in between steel substrate and outer aluminum layer. The intermetallic layer, which is and alloy of aluminum and iron, is produced during the immersion of the steel base in molten aluminum. This layer is brittle in nature; therefore, it is desired to keep the thickness of this layer to a minimum (Awan and Faiz, 2006). In hot-dip aluminizing with pure aluminum, such as the stock used for this investigation, the interlayer is thick and exhibits finger-like columnar crystal growth into the steel (Kimoto, 1999). SEM investigations illustrated that these finger-like features are composed of Fe_2Al_5. Studies showed that the presence of silicon in the molten aluminum decreases the thickness of the intermetallic layer and promotes the formation of a cubic Fe_3Al phase. The thickness of intermetallic layer may be also

associated with the carbon content of the steel substrate; as the carbon content increases the thickness of this layer decreases. Since aluminized steel Type 2 is produced by low carbon steel and nearly pure aluminum coating with no silicon, the intermetallic layer has an appreciable thickness, in order of 15 μm. As shown later, fracture of this brittle layer is a conspicuous manifestation of forming strain in the aluminized steel evaluated here.

1.4.2 Formability of Metal-Coated Steel Sheets

In order to study the effect of bending on aluminized steel in the present investigation, flat metal sheet stock was hemispherically indented to various radii (Chapter Four). The deformation and strain analysis of stressed regions under that complex biaxial regime is in progress and detailed analysis will be presented in the future. That analysis will be based in part on prior work on deformation of coated steel. For example, comparable studies have been done by Gupta and Kumar (2005) on formability of galvanized interstitial-free steel. Galvanized steel is produced by hot-dipping a steel substrate in molten zinc (450 C - 460 C) to form an intermetallic bond between the zinc coating and the steel. As indicated by the authors, "interstitial-free steel is produced by addition of titanium and/or niobium to an extra low carbon grade steel to precipitate interstitial carbon and nitrogen atoms" (Gupta and Kumar, 2006). Such materials are commonly used in the automobile industry due to their formability and high temperature corrosion resistance. In this investigation, Hecker's simplified technique which includes three steps: "grid marking the sheet samples, punch stretching the grid marked samples to failure or onset of localized necking, and measurement of strain"(Gupta and Kumar, 2006). Grid marking of samples was done by printing a circle on the surface of the sheet before punch stretching. Samples were punched using

hemisphere dies. After stretching the sheet the grid circles turned into ellipses. To obtain the strain distribution of formed samples, longitudinal strain of ellipses were measured. It was found that the ellipse which is located right under the punch suffers from a minimal strain. The result illustrated that the strains of uncoated sheets are higher than coated sheets. This is due to presence of a brittle intermetallic Fe-Zn layer. A similar method will be applied in future work to analyze the strain of dimpled aluminized steel specimens. Appendix D illustrates the work in progress to establish the relationship between the bending radius and strain in dimpled cells.

1.4.3 Corrosion Mechanism of Aluminized Steel

A recent review of the corrosion behavior of aluminized steel has been conducted by Caseres (Caseres, 2007). Highlights of that work are excerpted and summarized in the next indented section, paraphrasing as appropriate:

> Legault and Pearson (1978) conducted a five-year investigation on atmospheric corrosion of aluminized steel Type 2. In that investigation aluminized steel test panels with uncoated cut edges (exposing the base steel) were exposed to industrial and marine environment. Small (~0.2 μm/yr) and moderate (~0.45 μm/yr) corrosion rates were observed in industrial and marine environments, respectively. The cut edges were free of corrosion in marine environments and illustrated rust formation in industrial environments due to insufficient galvanic protection to the exposed steel (Legault and Pearson, 1978).
>
> Similar specimens were tested by Townsend and Borzillo (1987) in severe marine, moderate marine, rural, and industrial environments for 13 years.

The authors concluded that in aggressive environments, the aluminized coating is anodic to the exposed steel where chloride ions impair the passivity of aluminum. However, in industrial and rural atmospheres the aluminized coating passivated so that little to none galvanic protection to the underlying steel was noted (Townsend and Borzillo, 1987).

Johnsson and Nordhag (1984) also performed a four-year investigation to compare the sacrificial corrosion performance of several metallic coatings on steel exposed to atmospheric environments and seawater. Weight loss measurement was used to determine the corrosion rates of uncoated cut edges aluminized steel specimens with and without scribe marks, exposing underlying steel. The corrosion of aluminized steel even after one year was mostly in form of pitting, especially in a marine atmosphere. The investigation showed that except in marine environments, the aluminized steel without scribe marks outperformed the galvanized steel. The scribed specimens demonstrated the poor galvanic protection of the aluminized coating to the exposed steel in all environments and seawater, in the form of heavy red rust formation along the cut edges and at the scribe mark (Johnsson and Nordhag, 1984).

The majority of the studies on galvanic corrosion of aluminized steel were conducted by atmospheric exposure or by immersion in highly aggressive solutions. “Limited information exists on the galvanic behavior of aluminized steel with coating breaks exposed to fresh waters of varying scaling tendencies with moderate chloride contents, where galvanic protection may not take place at all” (Caseres, 2007).

Therefore, further research was conducted by the University of South Florida to address these issues, in the form of the investigation summarized in section 1.4.4.

Another recent investigation for methods to increase the corrosion durability of aluminized steel was conducted by Hong et al., (2002) .The investigation concluded that the addition of 1% Cr to aluminum coating increases the durability of aluminized steel Type 2. In fact, addition of Cr in the coating produces $Al_{13}Cr_2$ intermetallic layer which replaces Al_5Fe_4 layer. In this experiment samples were exposed to 3.5% NaCl solutions at room temperature. It was found that in aluminized steel with no addition of Cr, the outer aluminum coating initially corroded, followed then by the intermetallic layer (Al_5Fe_4). In samples with 1% Cr coating the aluminum layer also started to corrode first; however, corrosion stopped when it reached the intermetallic $Al_{13}Cr_2$ (Hong, 2002). Therefore, addition of Cr has a positive impact on the durability of aluminized steel materials.

1.4.4 Previous Studies Conducted by the University of South Florida

An investigation just completed at the University of South Florida (Caseres, 2007) addressed the issue of corrosion behavior of aluminized steel Type 2 with coating breaks (made by milling the aluminized steel sheet) of significant size (2 mm to 2 cm in diameter), compared with that of an unblemished aluminized steel surface. In that investigation samples were exposed to the same solutions used in the present work. The main findings are summarized in the following:

- An extremely low corrosion rate was detected for aluminized steel stock with no coating breaks exposed to solutions with moderate Cl content and high alkalinity/high hardness with consequently high scaling tendency. In solutions with moderate Cl content and low alkalinity, early pitting of the outer aluminized layer and strong

surface discoloration were observed. However, discoloration resulted from a momentary pH increase of the solution early on. In conditions where the pH remained near neutral, discoloration was delayed.

- In solutions with high scaling tendency and moderate chloride content, intense early steel corrosion at both small and large coating breaks was observed. The solution was benign and did not promote passivity loss of aluminum, so no cathodic protection of the exposed steel took place. However, in several instances there was delayed activation of the aluminum after long exposure times (e.g. 2,000 hrs), after which cathodic protection of the exposed steel took place. Little or no steel corrosion was observed in solutions aggressive enough to cause early passivity breakdown of aluminum.
- No clear pattern was established between corrosion rates and the size of the coating break.

The major objective of previous studies was to predict the corrosion behavior of flat stock aluminized sheet as a function of the scaling tendency in simulated natural waters, whereas, this investigation seeks to predict the corrosion performance of formed aluminized steel exposed to various bending stresses. As noted earlier, formed samples have micro breaks on the surface due to lack of ductility of brittle intermetallic interface. Formed samples are representative of conditions in corrugated and ribbed pipes which are also exposed to bending stresses during manufacturing.

In previous studies it was shown that large coating breaks, intentionally created on the surface of metal, would dominate the corrosion performance of the system. These breaks are significantly larger than those microfissures created due to bending stresses;

therefore, the corrosion trends predicted for large coating breaks may not be representative of the behavior of bent samples with small micro cracks. That issue will be investigated here.

1.5 Objective of This Investigation

This work aims at determining the corrosion behavior of mechanically formed aluminized steel Type 2. The microstructural aspects of mechanical distress upon bending as a precursor to corrosion development are characterized. Specimens with various bending radii of curvature are electrochemically assessed in waters of varying scaling tendencies with moderate chloride content, resembling compositions typically found in inland Florida waters. This investigation is in progress and initial findings are presented here, to be amplified in the future as additional information is developed.

1.6 Approach

To isolate the effect of bending, a set of aluminized steel samples are bent to various radii and are examined under environments representative of field conditions. The corrosion rate of these samples is monitored by visual inspection and electrochemical impedance spectroscopy. Also, in future work, the corrosion of existing field and factory samples will be analyzed and characterized.

The investigation was conducted in two stages. A series of preliminary experiments were made using simply bent specimens and sponges saturated with the test solution or epoxy-cast stoppers to delimit the zone of the bent region exposed to the test solution. Those experiments served as ranging tests to obtain initial indication of the

effect of bending on corrosion performance. However, the preliminary tests also indicated that it was very difficult to delimit the portion of the specimen being exposed, with consequent uncertainty due to formation of crevice corrosion in regions of the specimen not related to the bent condition.

Consequently, specimen design was changed to use flat sheet stock dimpled at the center to a controlled deformation degree. That design avoided unwanted crevice corrosion and proved to be a reliable and simple procedure for determining effects of forming on corrosion performance. The main corrosion characterization technique used was Electrochemical Impedance Spectroscopy (EIS).

Findings from the preliminary and the final specimen designs are presented in separate chapters.

Chapter Two

Preliminary Experiments and Results

The following describes the procedures and findings of the preliminary investigation of the effect of simple bending on corrosion of aluminized steel. Additional details have been presented elsewhere (Akhoondan and Sagüés, 2007). It is noted that these experiments were semiquantitative in nature, and generally aimed at developing an adequate test set up for reliable testing. The final method, using dimpled or "deep drawn" specimens, is detailed in the next chapters.

2.1 Bending Process

In the preliminary experiments, 16-gage (1.58 mm thick) aluminized steel sheet was cut to rectangular strips, typically, 2-in x 6-in, 2-in x 3-in and 1-in x 6-in. Next, 2-in x 6-in, and 1-in x 6-in samples were bent to different radii using a bending jig.

For sharper bends, after specimens were pre-bent as above, U shaped strips were pressed in a vise to obtain a sharper radius. The 2-in x 3-in strips were not bent, but used instead as flat specimens to compare the corrosion behavior of bent and unbent materials. The specimens were classified depending on the bending radius as sharp-bend (r=1.5 to 3 mm), mid-bend.(r= 3 to 5 mm), large (r=5 to 15 mm) and flat (r > 50 mm).

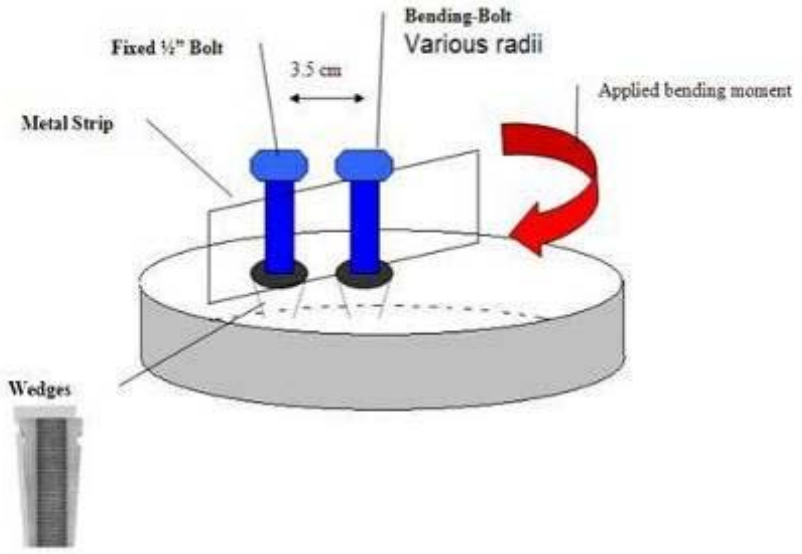

Figure 2-1. Bending Process of Metal Strips

2.2 Electrochemical Cell Set Up and Test Solution

Two types of electrochemical cell systems were designed to conduct the preliminary experiments. The electrolyte chosen for both cells was a normally protective solution (designated "P") used in the previous work by Caseres (Caseres and Sagüés, 2005). This solution tends to precipitate a protective carbonate film on the metal, but it also contains ~ 372 ppm chloride ions. The solution P is made from de-ionized water of resistivity > 10^6 Ω-cm , to which $NaHCO_3$ HCl, and $Ca(OH)_2$ are added as indicated in Table 3-1. The pH stayed almost constant in the range of 8 to 8.5 during the experiment. The solution in the cells was naturally aerated and the temperature was 21-24 ^oC.

2.2.1 Sponge-Cell System

The sponge-cell system represents conditions that might be encountered in the outer (soil side) surface of aluminized steel culvert pipes. In this case, the sponge acts as a porous medium which absorbs, transfers and holds the solution to the surface of metal.

Sponge-cell samples were assembled as in Figure 2-2**.** In order to prevent exposing the cut sheet edges, which because of the exposed steel are not representative of the main surfaces, they were covered with a two component (EP-308, Thermoset Plastics Inc., Indianapolis, IN) industrial epoxy resin and allowed to set for 24 hrs. Then the samples were degreased with ethanol and acetone, and stored in a desiccator before use. A low impedance activated titanium reference electrode (Castro et al., 1996) was firmly embedded in the sponge 1 cm away from the bend, and periodically calibrated against a saturated calomel reference electrode (SCE). The tip of the titanium reference electrode used for the EIS tests is embedded in the sponge firmly 1 cm away from the bend. The counter electrode is a stainless steel wire which is in contact with the electrolyte.

Open circuit potential monitoring as well as periodic Electrochemical Impedance Spectroscopy (EIS) tests (frequency range from 100 kHz to 1 mHz using sinusoidal signals of 10 mV rms amplitude) were conducted by Gamry™ PCI4-300 potentiostat on this system to measure the corrosion rate and compare the results from both flat and bent samples. The type and number of samples tested in the sponge-cell experiments are listed in Table 2-1.

Table 2-1 Inventory of Specimens Tested in the Sponge-Cell

	Flat	Sharp-Bend	Mild-Bend	Exposure Time
Total No. of Specimens Tested	4	3	9	288 – 840 hrs
Specimens not showing crevice effects (results reported for these only)	2	2	3	

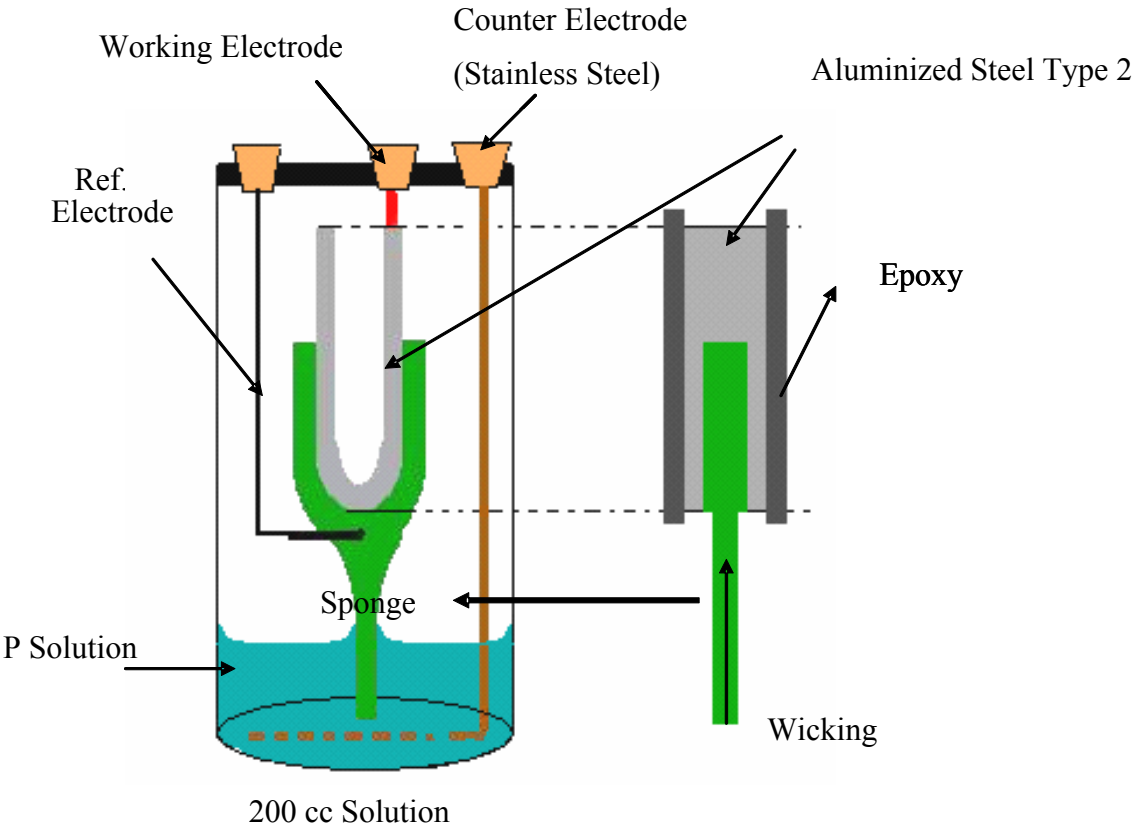

Figure 2-2. Sponge-Cell Configuration-Bent Samples

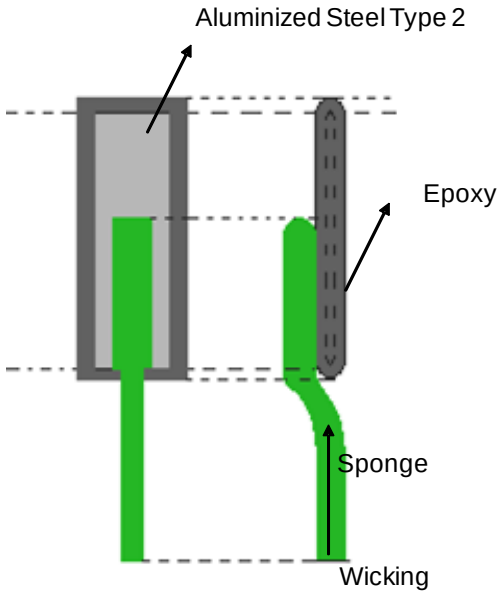

Figure 2-3. Flat Samples in Sponge-Cell Set Up (Exposed Area 12 cm^2)

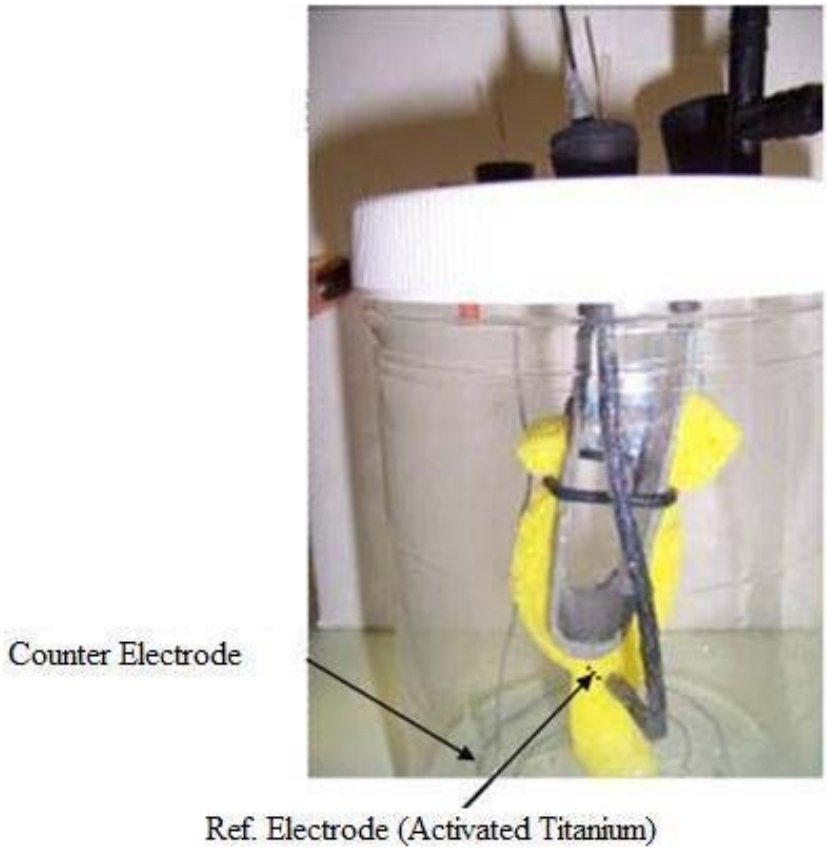

Figure 2-4. Photograph of a Sponge-Cell with a Bent Sample

2.2.2 Immersion-Cell System

The immersion-cell system was designed to represent conditions that might exist in the inner surfaces of pipes, which are exposed to flowing or standing water. The same bending process described earlier was used for these samples as well. However, the edges of specimens were completely covered with a highly adherent metallographic mount epoxy (Buehler Epoxicure, Buehler, USA), instead of the EP-308 industrial epoxy which tended to lose adherence early during the tests. Figure 2-5 illustrates the configuration of the immersion-cell specimens. An activated titanium reference electrode as described earlier was placed in the solution 1 cm away from the specimen and periodically

calibrated against an SCE. The electrolyte was the same as used in the sponge-cell system. The type and number of samples tested in the sponge-cell experiments are listed in Table 2-2.

Table 2-2 Inventory of Specimens Tested in the Immersion-Cell

	Mild	Sharp	Exposure Time
No. of Specimens	1	3	408 – 1512 hrs
Specimens not showing crevice effects (results reported for these only)	1	3	

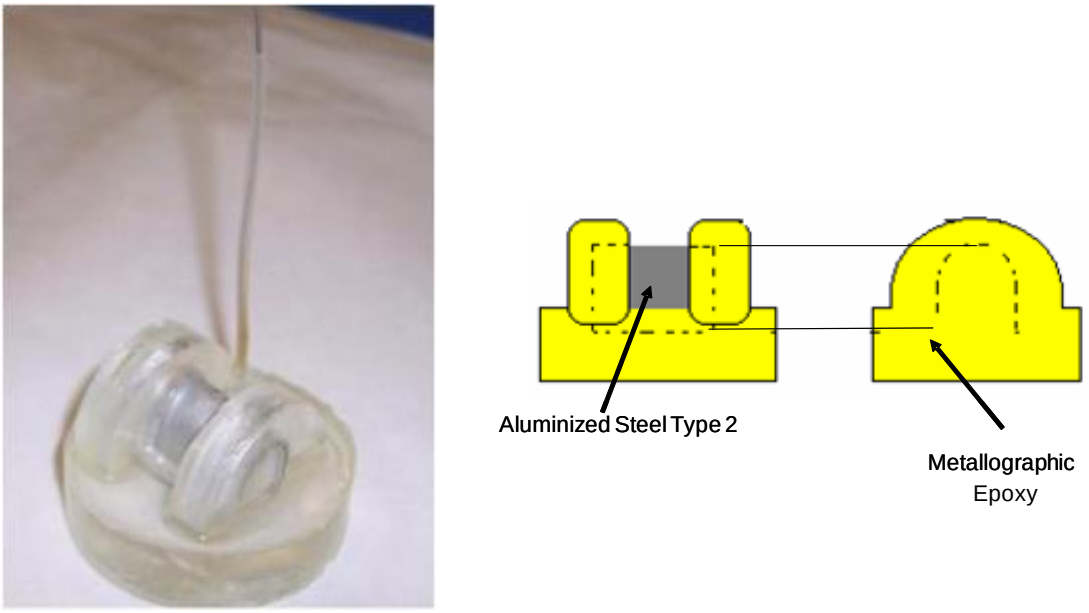

Figure 2-5. Configuration of a Mild Bend Specimen for the Immersion-Cell System

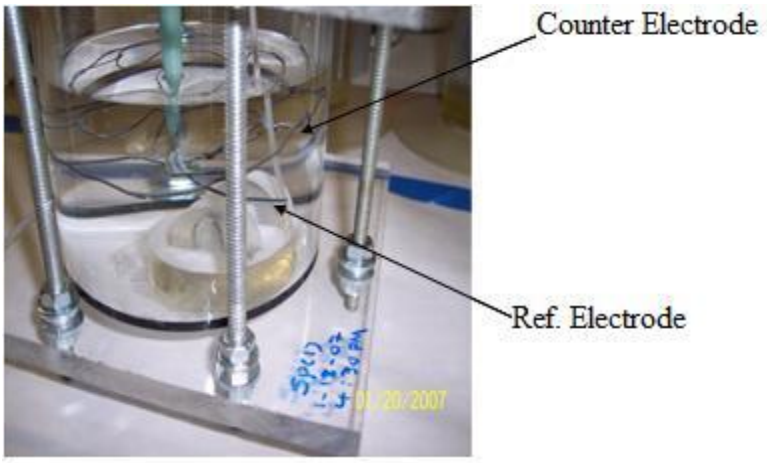

Figure 2-6. Test-Cell of the Immersion-Cell System

2.3 Results and Discussion

Many of the specimens in the sponge-cell systems developed crevice corrosion due to poor performance of the Ep-308 epoxy which allowed disbondment and moisture intrusion at the epoxy-metal interface. Specimens showing those symptoms were discarded. Therefore, even though 15 samples were exposed in the sponge-cells, the results of only six samples were taken into account.

2.3.1 Open Circuit Potential Trends

The Open Circuit potential (E_{OC}) graphs illustrated that in both sponge-cell and immersion-cell systems, flat specimens tended to develop the lower potentials (approaching E_{OC} values typical of aluminum). In contrast, bent specimens tended to develop higher E_{OC} values, thus reflecting a mixed potential approaching the E_{OC} value of steel, a sign of preferential steel corrosion in a steel-aluminum couple (Caseres and Sagüés, 2005). Typically, the E_{OC} of pure aluminum in neutral aerated water is in the order of -1 V (SCE), while E_{OC} of actively corroding steel in aerated conditions is in the order of -0.6 V (Caseres and Sagüés, 2006). The polarizability of passive aluminum is

very high (Caseres and Sagüés, 2006), so in an Al-steel couple even very small amounts of exposed steel are likely to result in a mixed potential approaching that of only steel (Caseres and Sagüés, 2006).

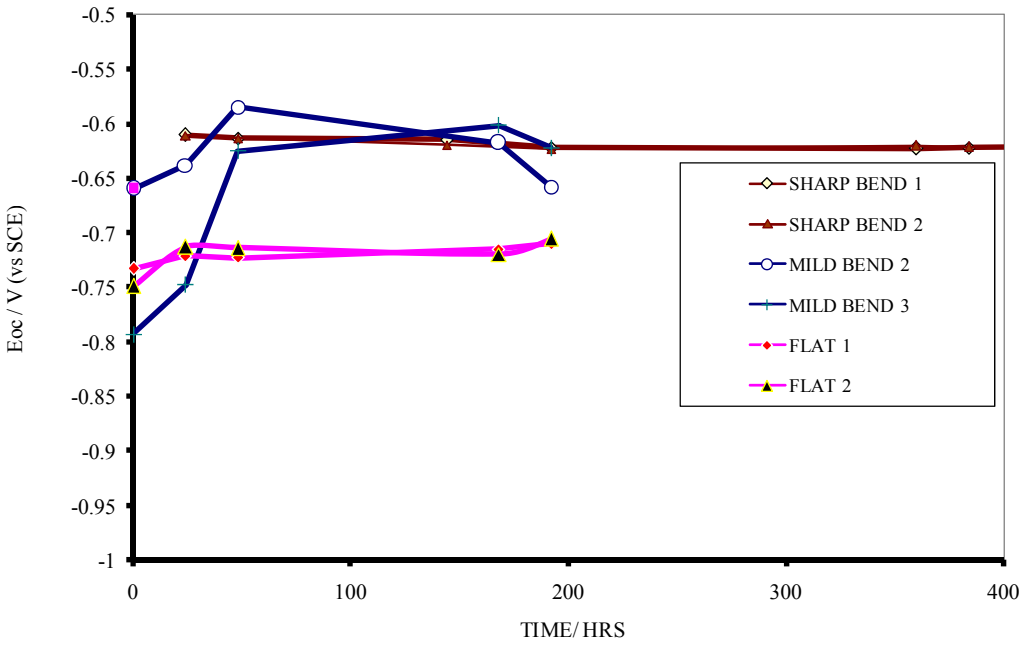

Figure 2-7. E_{OC} Trends with Exposure Time in Sponge-Cell System

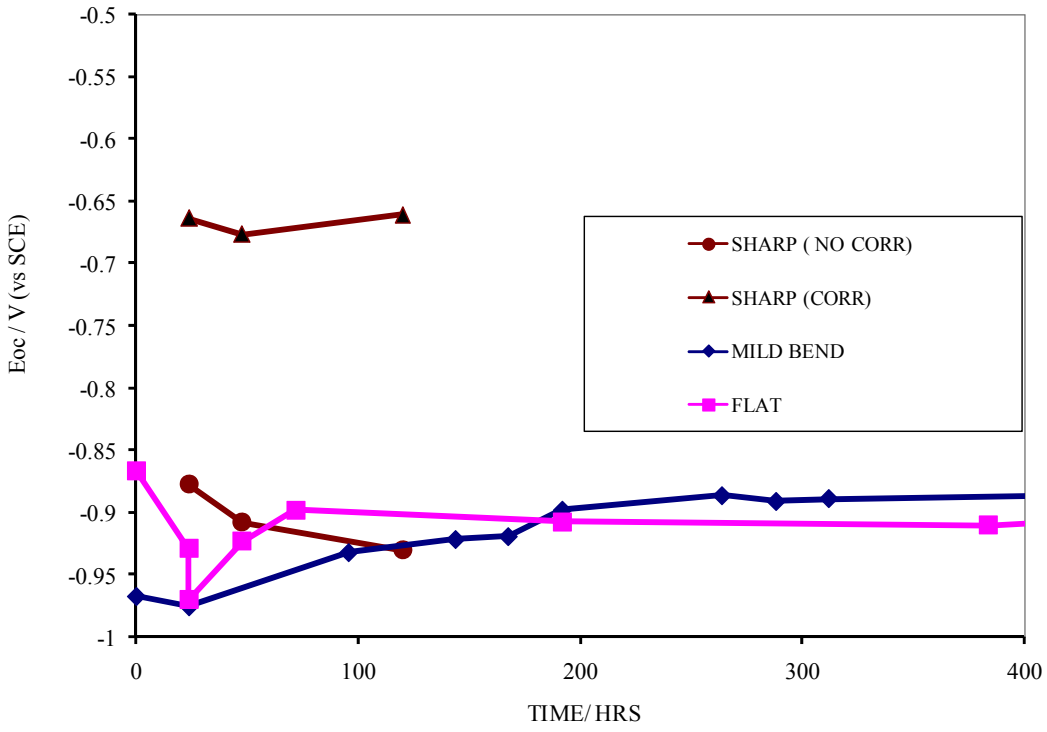

Figure 2-8. E_{OC} Trends with Exposure Time in Immersion-Cell System

2.3.2 EIS Trends

The EIS results for the sponge-cell system are shown in Figure 2-9 to 2-11. Also, EIS results are illustrated in terms of the corrosion current I_{Corr} in Figure 2-12. Apparent Rp values (Rpa) were assumed to be equal to the impedance modulus |Z|@ 0.001 Hz minus the value of the solution resistance. The solution resistance Rs was assumed to be equal to |Z| @ 10^{5} Hz. The underlying principles are described in standard literature sources and course summaries (Sagüés, 2006).

The corrosion current I Corr was calculated from

$$I\ Corr = B/(Rpa - Rs) \qquad Eq(1)$$

where B = 26 mV (Typical value of the Stearn-Geary constant for corroding steel (Jones, 1996).

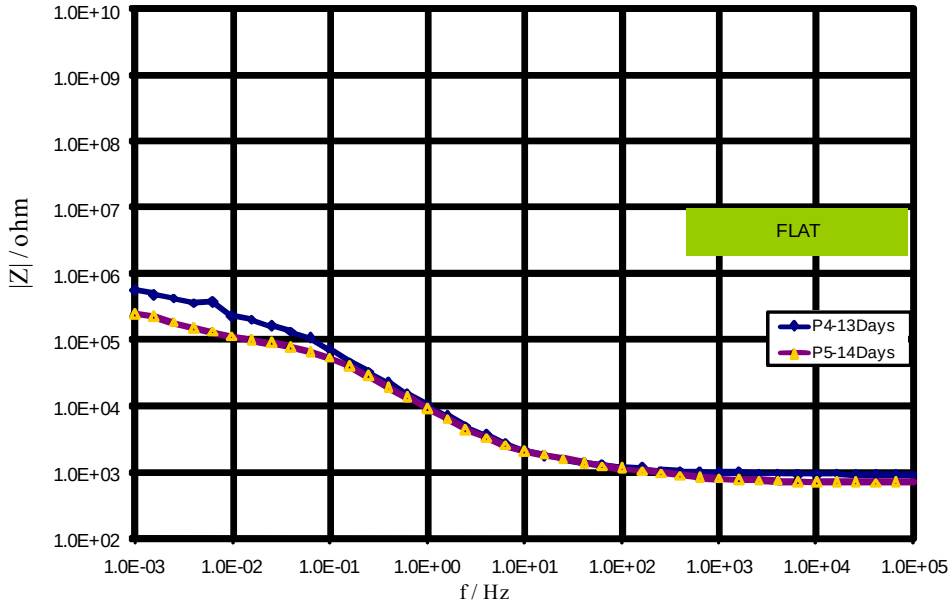

Figure 2-9. EIS Behavior of Flat Specimens in Sponge-Cell System

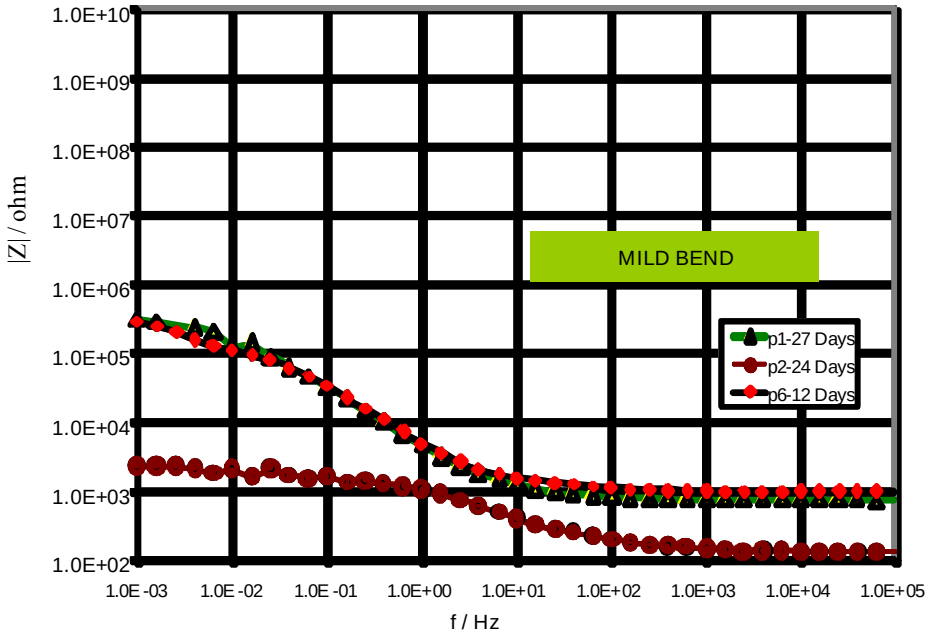

Figure 2-10. EIS Behavior of Mild Bent Specimens in Sponge-Cell System

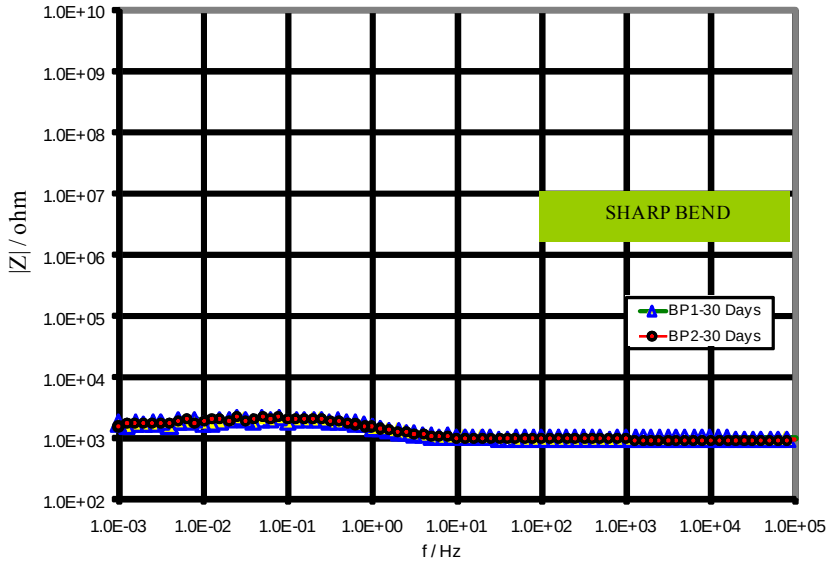

Figure 2-11. EIS Behavior of Sharp Bent Specimens in Sponge-Cell System

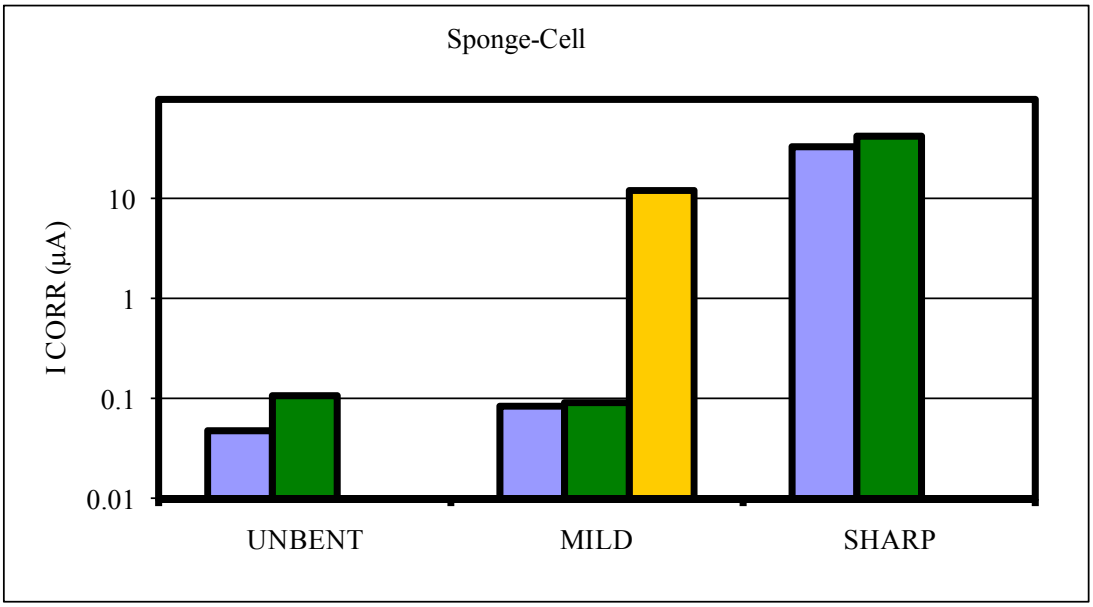

Figure 2-12. I_{Corr} Trend of Specimens with Various Radii in Sponge-Cell System

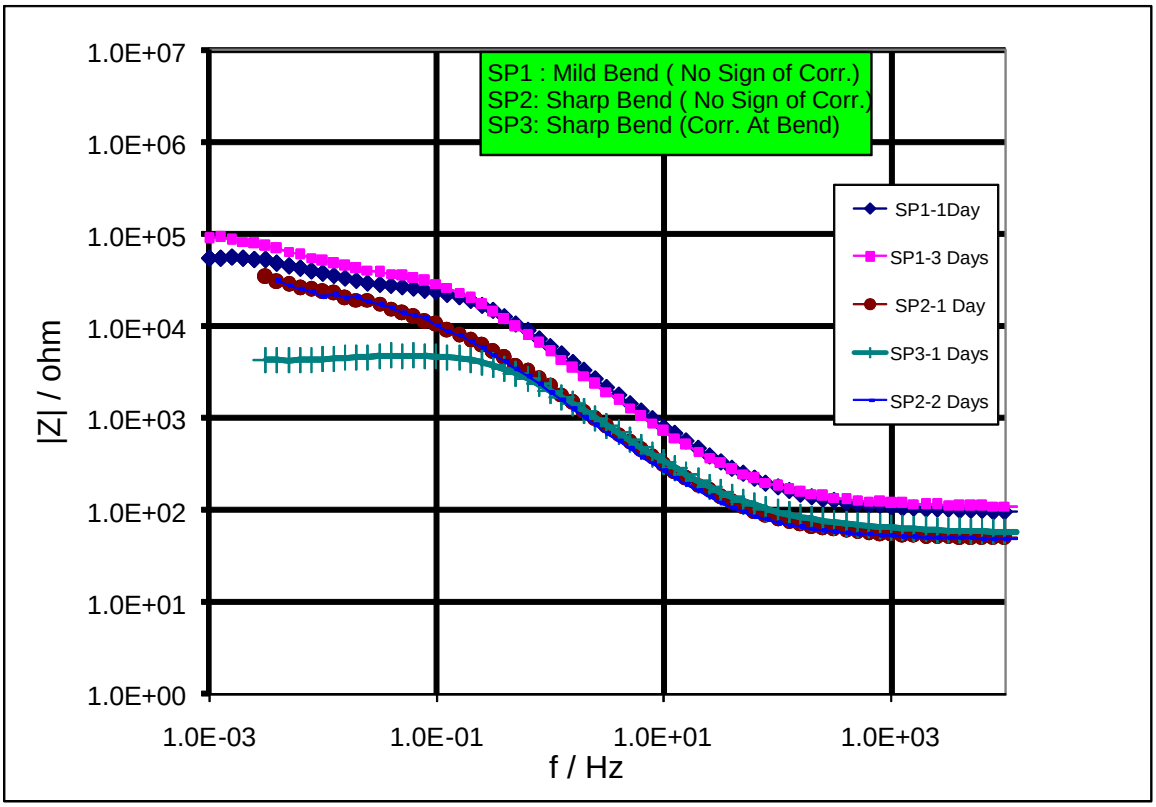

Figure 2-13. EIS Behavior of Bent Specimens in Immersion-Cell System

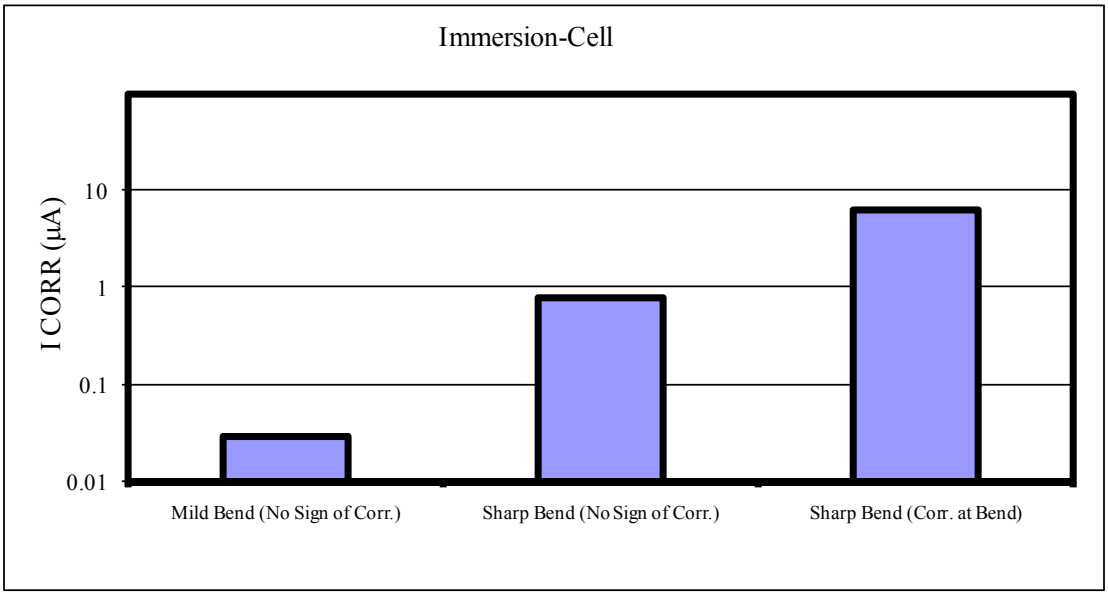

Figure 2-14. I_{Corr} Values of Mild-Bend and Two Sharp-Bend Specimens in the Immersion-Cell System

In both systems unbent specimens had the greatest polarization resistance (Rp) values. Mild bend specimens had smaller Rp values compared to those of the flat samples. Finally, sharp-bend specimens had the smallest Rp compared to mild bend and unbent specimens. Sharp-bend specimens have the highest I Corr (33-43 μA) values. As the severity of bending increased the apparent corrosion current also increased. Results correlated with the E_{OC} trends.

2.3.3 Direct Observation of Corrosion

The bend region was covered in the sponge-cell specimens so it was not amenable for direct examination early in the test. sponge-cell specimens were not opened until late in the test exposure when extensive corrosion had taken place, so those results will not be considered. In the immersion-cell system, no crevice corrosion was observed in any of the samples. A sharp-bend specimen clearly showed corrosion signs (red rust) at the bend region soon after exposure began.

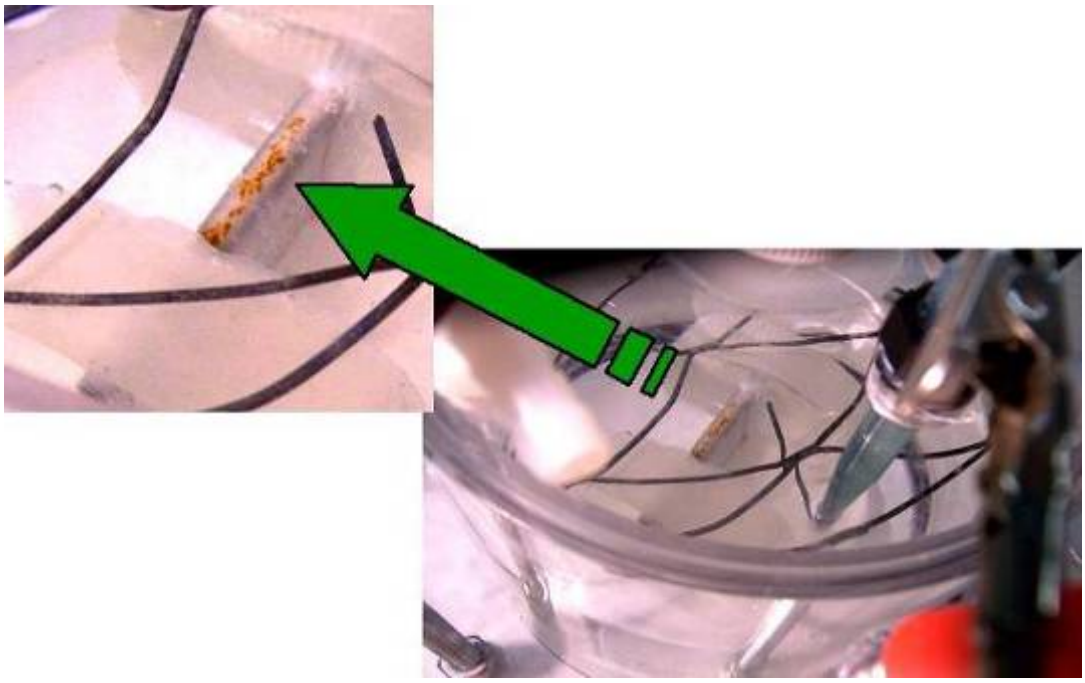

Figure 2-15. Immediate Sign of Corrosion at Bend Region in Immersion-Cell Samples

2.4 Conclusions Obtained From Preliminary Experiments

- Preliminary findings indicated preferential deterioration in bent samples and damage associated with mechanical distress.
- E_{OC} measurements in general showed more positive potentials for sharper bends, indicative of exposing steel at coating breaks.
- Sharp-bend specimens had highest corrosion rates compared to mild bend and flat specimens.
- Exposed steel (at microfissures due to the bending process) in a sharp-bend aluminized steel specimen experienced intense corrosion early in the test.
- The above findings were affected by significant uncertainty due to artifacts that led to the development of the next generation test-cell.

Chapter Three

Deep Drawn Aluminized Steel Experiments-Methodology

The following describes the procedures for the main phase of this investigation, which resulted in the development of an improved dimpled specimen configuration. This work evolved from the preliminary study of the effect of simple bending on corrosion of aluminized steel described in the previous chapter.

The preliminary experiments showed that crevice corrosion occurred frequently at bent specimen edges, where the deformed surface needed to be delimited. That limitation was overcome in the present design by using flat specimens with a central controlled-deformation dimple. Surface delimitation took place at the flat portion of the specimen, where crevice formation was less common due to use of a gasket assembly perfected earlier (Caseres, 2007).

The work also seeks to quantify the effects of forming on microstructural damage, for later relating that damage to extent of resulting corrosion. Experiments to date examine the effect of simple (uniaxial) bending and methodology, and results of that phase of the work are presented here. The effects of biaxial bending, as in dimpling, have only been examined in exploratory tests (see Appendix D) and will be explored in detail in the future.

Additional details of this phase of the work have been accepted for publication elsewhere (Akhoondan, Sagüés and Caseres, 2008).

3.1 Dimpling Procedure

Circular 16-gage aluminized steel specimens with exposed area of 12.56 in^2 (82 cm^2), and with minimal as-received surface distress were hemispherically indented at the center using stainless steel ball-bearing balls with diameters of 1 in (2.54 cm) , 3/4 in (1.90 cm), or 9/16 in (1.43 cm) as shown in Figure 3-1. The indentation was made by pressing the bearing ball, socketed in a steel plate into the initially flat specimen. An indented Teflon plate was used to protect the convex face of sample until full hemispheric penetration was achieved. The convex face was the one later exposed to the test solution. Afterwards, the specimens were cleaned with ethanol and acetone, and stored in a desiccator prior to immersion. Figure 3-3 shows the appearance of the dimpled specimens. Control flat specimens without surface indentation were also used for comparison. Multiple specimens were prepared for duplicate testing.

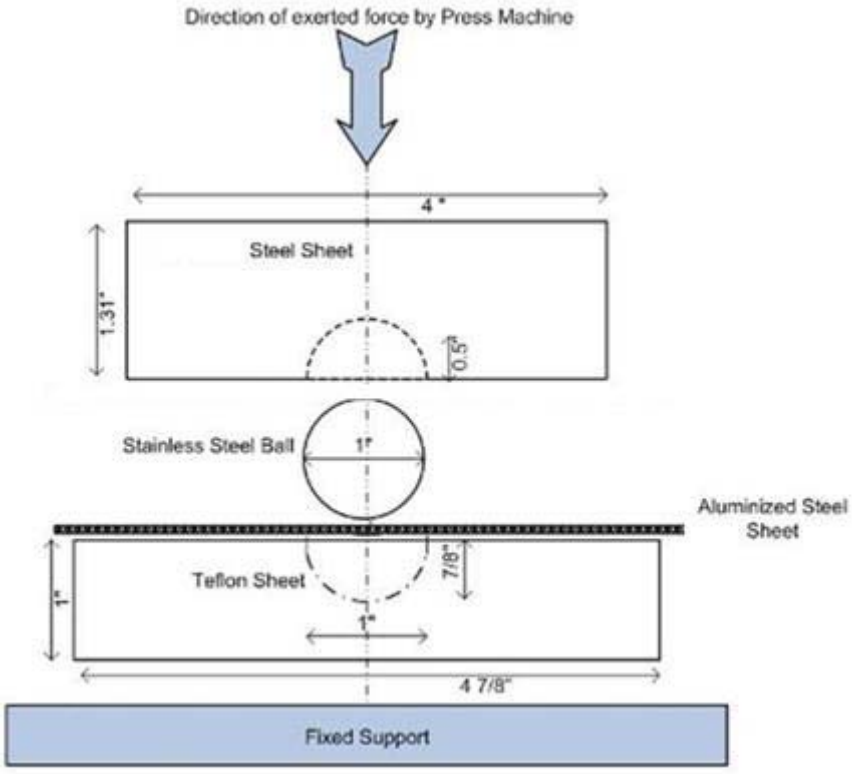

Figure 3-1. Dimpling Specimens Using a Press-Sketch Shows Dimensions for the 1-in Ball Case.

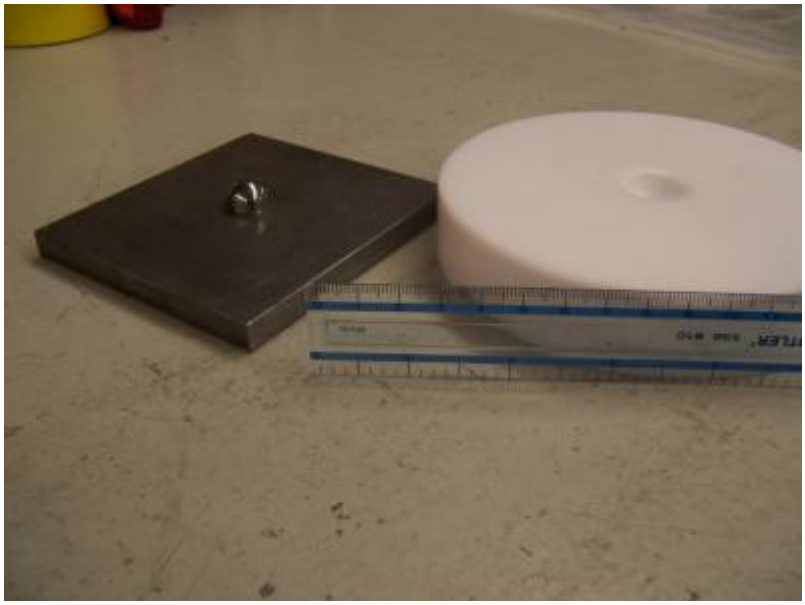

Figure 3-2. Forming Assembly Used to Dimple Specimens. (Picture shows the 9/16-in case).

Figure 3-3. Duplicate Aluminized Steel Specimens (Left to Right) 1-in, ¾-in, 9/16-in, and Flat

3.2 Immersion-Cell Experiment

A three-electrode test-cell (Figure 3-4) was designed for exposing horizontally the convex side of the specimen, where distress is expected to be worst because of the tensile

stresses. Corrosion of the concave side will be assessed in future experiments. A metal-metal oxide activated titanium mesh placed parallel ~6 cm from the specimen surface was used as a counter electrode. A low impedance activated titanium pseudo reference electrode 0.3 cm diameter and 5 cm long (Castro et al., 1996) was placed ~1.5 cm above the specimen's indentation and periodically calibrated against an SCE. All potentials reported here are in the SCE scale. Each test-cell was filled with 500 mL of solution, not replenished during the test for reasons explained below and in section 2.2.2.

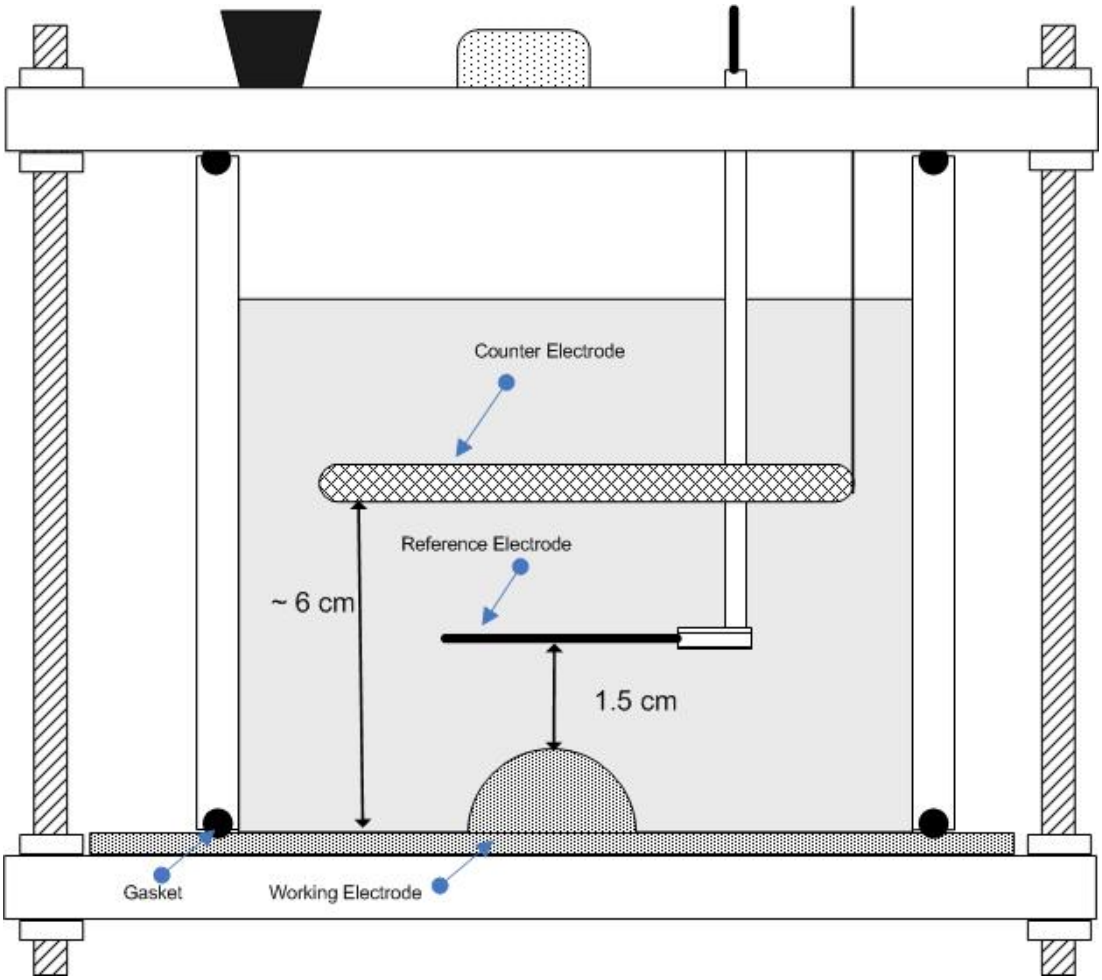

Figure 3-4. Three-Electrode Cell Configuration

The immersion tests were conducted in duplicate for each test solution, at 22±2˚C. Solution pH was verified, and E_{OC} was monitored The E_{OC} measurements were taken

nearly daily and plotted as function of exposure time to reveal transitions indicative of corrosion condition. EIS measurements were obtained at the E_{OC} with a Gamry™ PCI4-300 potentiostat in the frequency range from 100 kHz to 1 mHz using sinusoidal signals of 10 mV rms amplitude. The results for the first ~600 hrs and ~1,000 hrs of exposure are presented here for solutions C and P respectively as well as limited initial EIS data. Exposure continues and long-term performance will be presented in a subsequent publication.

3.3 Solution Compositions

Two test solutions (Table 3-1) were prepared from de-carbonated de-ionized water of resistivity > 10^6 Ω-cm combining reagent grade NaCl and NaOH (solution C of negligible carbonate precipitating tendency) and $NaHCO_3$, HCl, and $Ca(OH)_2$ (solution P of high carbonate precipitating tendency). These solutions are identical to those used by Caseres (Caseres, 2007), who showed that the Langelier Index was -5.9 for solution C and +1.50 for solution P, consistent with the observation of a powdery precipitate layer of $CaCO_3$ uniformly distributed on the specimen surface shortly after initiation of exposure. The test solutions in the test-cells were quiescent and naturally aerated through a small opening. As in previous work by Caseres (Caseres, 2007) and noted elsewhere (Akhoondan, Sagüés and Caseres, 2008), the relatively small electrolyte volume/total specimen area ratio was intended to be representative of, for instance, worst-case culvert pipe conditions with stagnant water on the pipe invert, or of occluded conditions for pore water on the soil side of a pipe.

Table 3-1. Solution Compositions and Properties

Solution	TA	TH	FC	BI	pH	Ca^{+2} mg/L	Cl^{-} mg/L
C (Control)	6	2	0	8	~7.4	0	372
P (Precipitating)	184	52	13	223	~7.4	200	
Preparation (Per 1 L of Solution)							
C	0.05 mL of 0.01 M Na(OH)						
	5.25 mL of 2 M NaCl						
P	100 mL of 0.1 M $NaHCO_3$						
	0.37 g of $Ca(OH)_2$						
	105 mL of 0.1 M HCl						

Legend: TA: total alkalinity (mg/L) of $CaCO_3$, TH: total hardness (mg/L) of $CaCO_3$, FC: free CO_2, σ: solution conductivity

3.4 Metallography

Microstructural assessment of mechanical distress due to bending has been performed to date with 16-gage (1.58 mm thick) Type 2 aluminized steel sheets simply bent to various extents. The bent region was mounted metallographically and examined with an optical metallographic microscope.

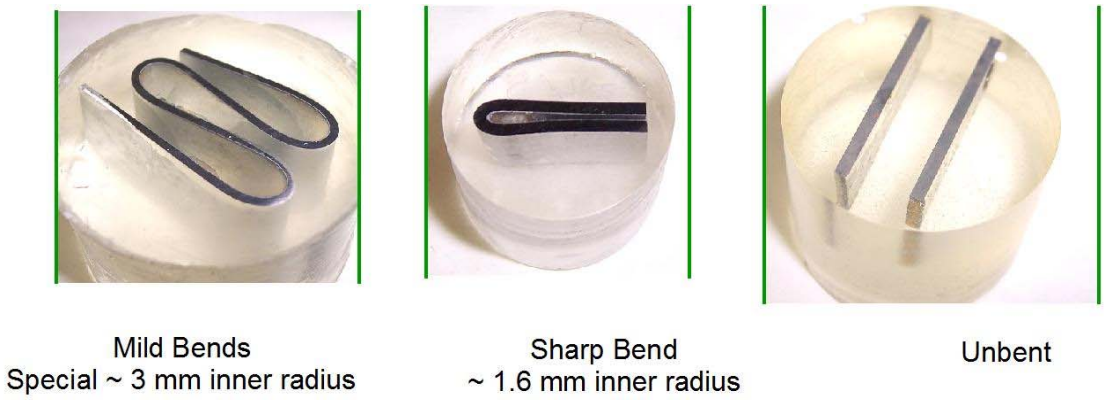

Figure 3-5. Simply Bent Metallographic Specimens

3.4.1 Metallography Process

To prepare the metallographic samples the following steps were executed: First, the specimens were cut out from the sheet stock using a manual hack saw and carefully avoiding marring of the surfaces; then the specimens were degreased with ethanol. Next, they were molded in (Buehler Epoxicure, Buehler, USA) metallographic epoxy.

After curing for 24 hrs, the specimens were demolded and were ready for grinding and polishing. Abrasive papers (SiC 80, 120, 600, 1200 grit, Struers Inc, USA) were used to grind the samples in a Buehler Ecomet III turntable. During grinding tap water was used as a lubricant. Then specimens were polished using (SiC 2400, 4000 grit, Struers Inc, USA) papers and a lubricant (D-P Lubricant, Blue, Struers Inc, USA) which is non-aqueous. Final polishing steps were conducted using a cloth (MD-Dac, Struers Inc, Denmark), with Dp Blue Lubricant and, and 1µm diamond paste (Dp-paste, P, Struers Inc, Denmark). An even force of about 20 N on a medium speed wheel was applied to accomplish a better result. A demonstration sample preparation was also made by Struers

(Struers Inc, USA) using automated equipment. After the samples were polished and cleaned, the cross section of the outer bent was examined at low magnification and digitized to determine local radius of curvature (Figure 3-6). The same regions were then examined at high magnification to determine the type and extent of distress, as exemplified in Figure 3-7.

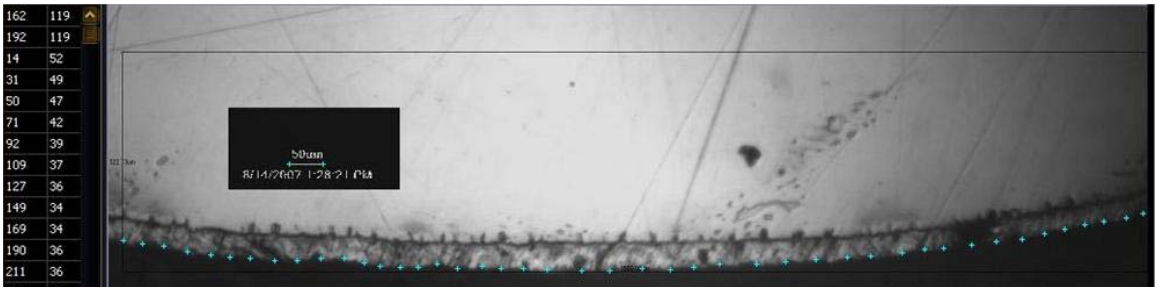

Figure 3-6. Example of Digitalized Image Used for Finding the Radius of Curvature

As it is explained in the next chapter, the calculated strain for each simply bent sample was obtained by assuming a constant neutral axis located at the center of metal. Future experiments and calculations will address the deformation of samples formed by spherical indentation as those explained in section 3-1. The analysis of such deformation is more complex, since these dimpled samples were exposed to biaxial stress. A more complete analysis is being investigated in continuation work.

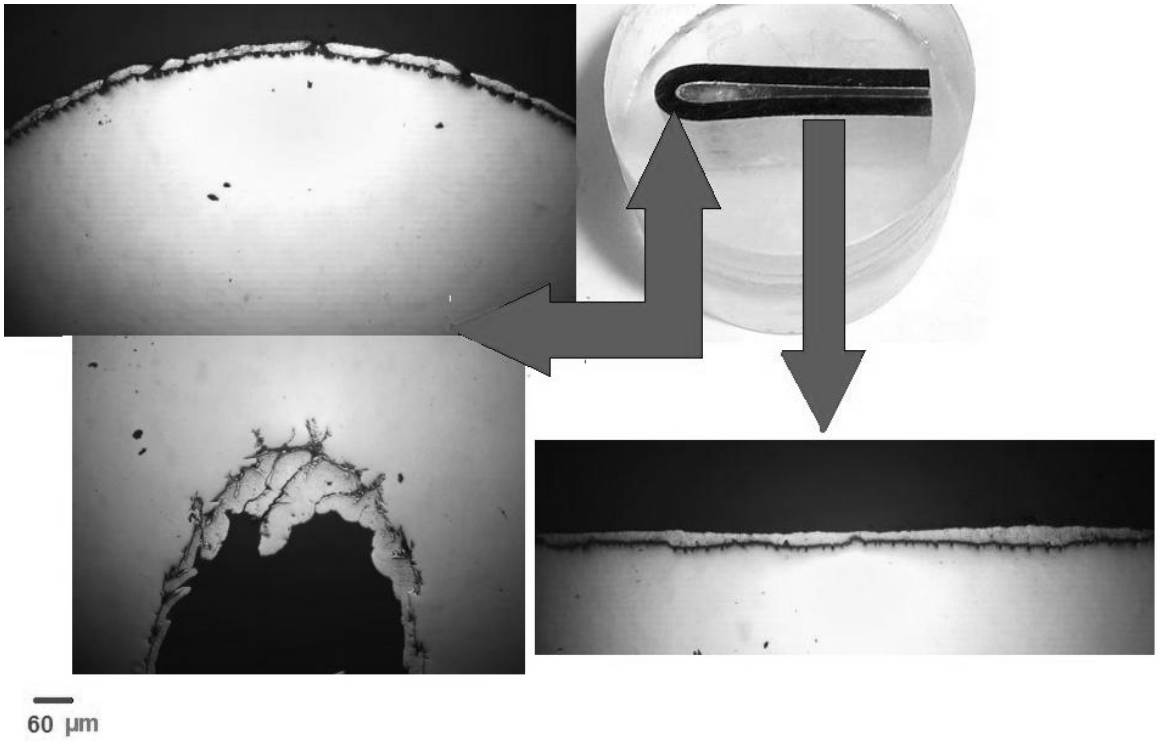

Figure 3-7. Effect of Bending on the Aluminum Coating of a Sharp Bend Sample. (Analysis emphasis was on the convex portion of the specimen; inner portion is shown for illustration of other forms of damage to be examined in the future).

Chapter Four

Deep Drawn Aluminized Steel Experiments-Results and Discussion

4.1 Metallographic Analysis

Figure 4-1 (left) shows a metallographic cross section of the as-received (flat) material showing the coating microstructure described in the Introduction. Figure 4-1 (right) shows the coating condition of a sharply unaxially bent sample (radius ~2 mm). The most notable feature is nearly completely brittle fracture of the intermetallic layer, as manifested by its many elongation gaps. The outer coating was much more ductile, with a few instances of ductile fracture such as that illustrated on the left side of Figure4-1, apparently originating at one of the larger brittle gaps of the inner layer.

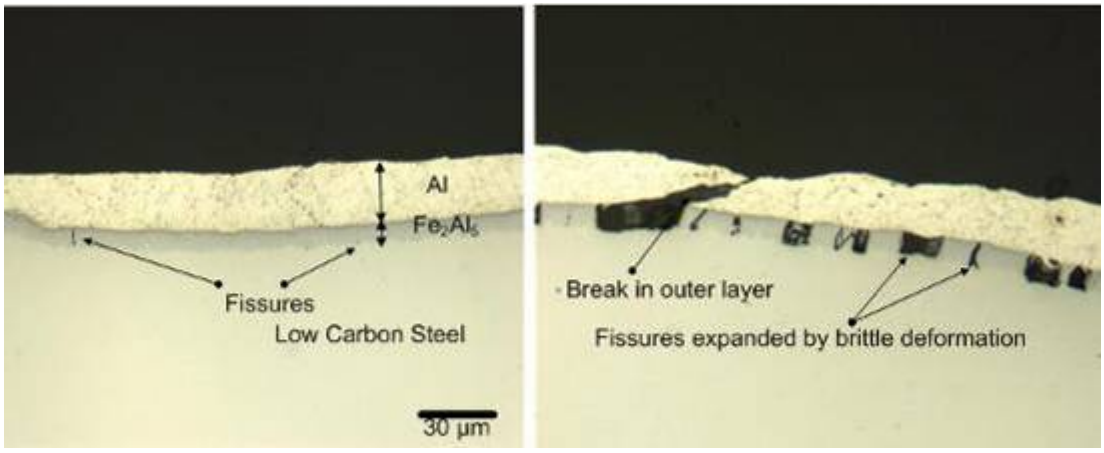

Figure 4-1. Aluminized Steel Metallography, Flat Specimen (left), Bent Specimen (right). Special Automated Sample Preparation Courtesy of Struers Inc.

The number and severity of fractures in the inner layer increased as the bending stress increased. For completely brittle fracture, the integrated gap length measured on a

line parallel to the perimeter, divided by the initial length (that is, the sum of the lengths of the remaining visible intermetallic segments) should equal the total strain at the outer fiber. To test that hypothesis, the strain ε_M calculated from measurements of the ratio of inner layer gaps to visible intermetallic length was compared with the strain at the outer fiber expected from the local macroscopic bending radius and the sheet thickness. For a simply bent sheet in which the neutral axis of metal sheet stays constant, the theoretical relationship between the strain of outer fiber and radius of curvature (Dieter, 1986) is:

$$\varepsilon_I = \frac{T}{2\left(R - \frac{T}{2}\right)} \qquad \text{Eq(2)}$$

where:

ε_I is the ideal strain

T is the thickness of the sheet (16-gage = 1.58 mm)

R is the outer bending radius

The derivation of Eq(2) is illustrated in Figure 4-2 and the following text. .

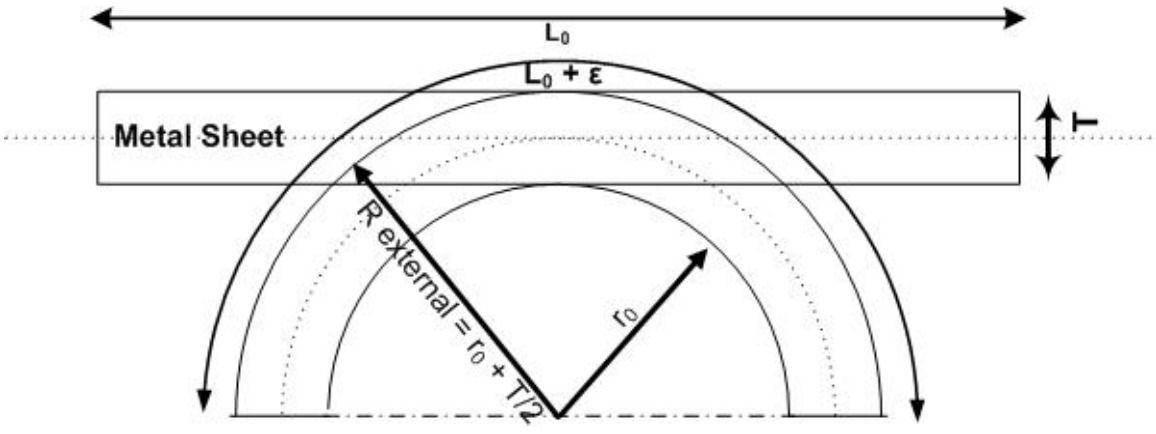

Figure 4-2. Strain and Radius Relationship

$R_{external} = r_0 + T/2 \quad \rightarrow \quad r_0 = R_{external} - T/2$

$\varepsilon_{external} = (L_0 + \varepsilon - L_0) / L_0 = (R_{external} - r_0)/ r_0$

$= (r_0 + T/2 - r_0)/ r_0$

$= T/2 / r_0$

$= T / [2 (R_{external} - T / 2)]$ which is the same as Eq(2).

Figure 4-2 compares the values of ideal outer fiber strain computed per Eq(1) from the radius of curvature (determined for various specimens from the low magnification micrographs) and the sheet thickness, and ε_M from the micrographic analysis of the intermetallic layer (Figure 4-5). Flat samples were assigned a radius > 50 mm in the graph. The results show good agreement between measured and expected strain, supporting the hypothesis of nearly completely brittle behavior for the inner intermetallic layer. Tests in progress address behavior of specimens bent by spherical indenting and ductile fracture of the outer layer, which will be reported in the future.

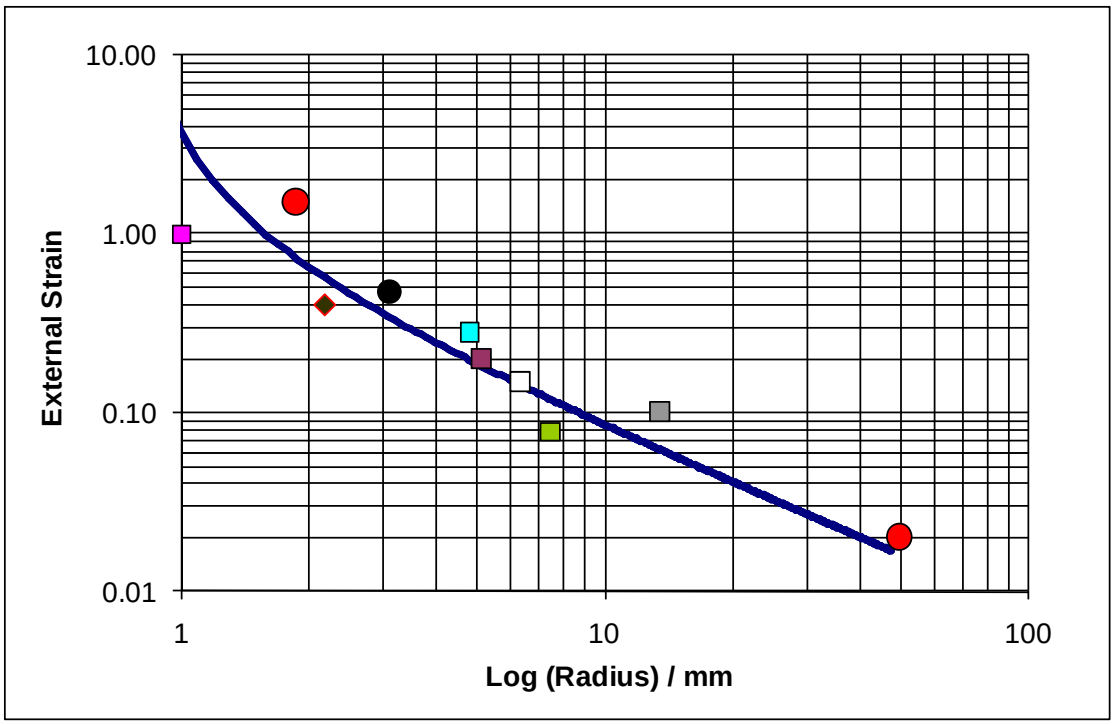

Figure 4-3. Outer Strain (ε_I per Eq(1), solid line) and ε_M per Micrographic Analysis of Intermetallic Layer gaps, symbols) as Function of Radius of Curvature for Several Samples

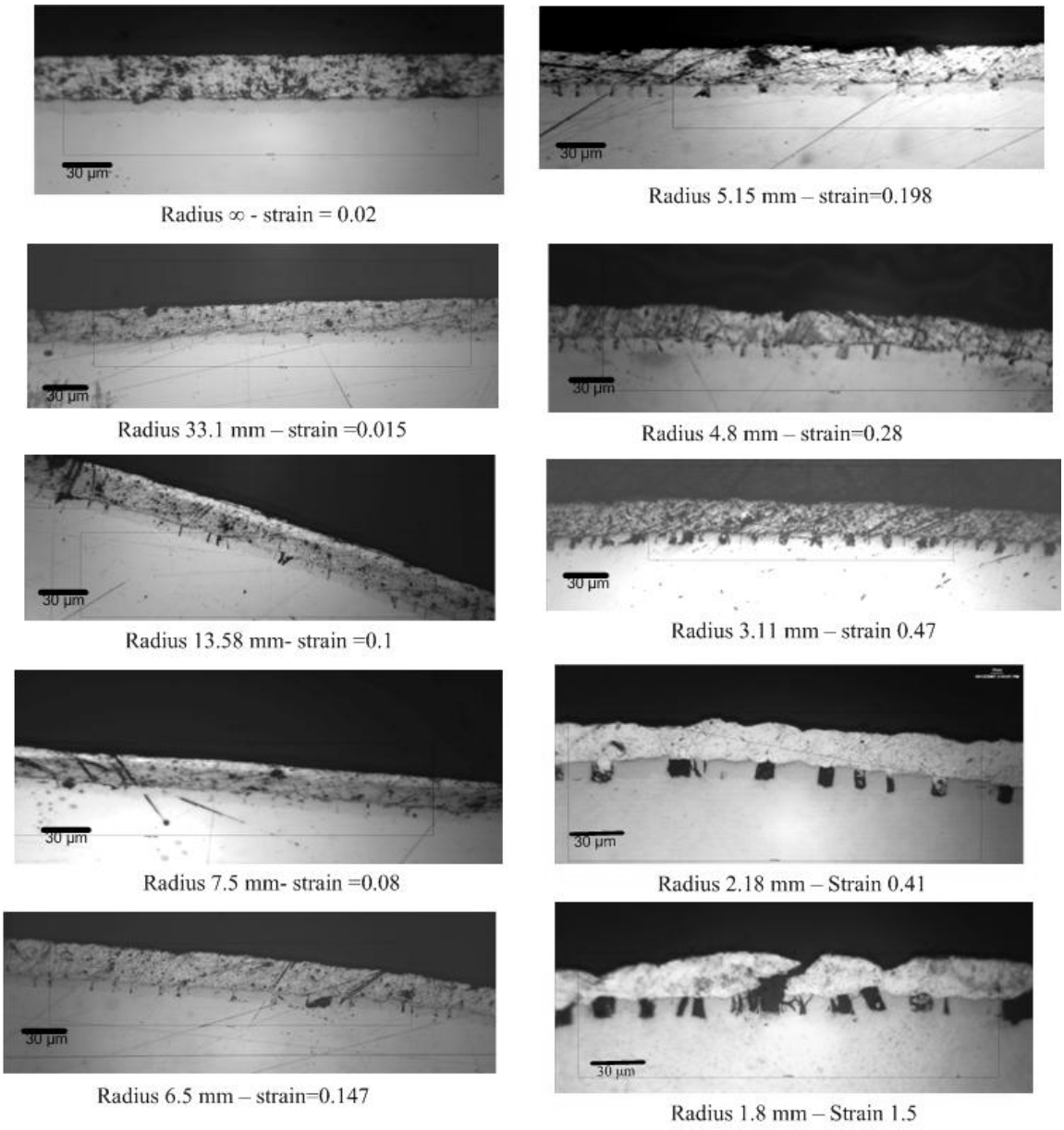

Figure 4-4. Selected Microscopic Photos of Outer Layer of Specimens Introduced in Figure 4-3

4.2 Direct Observation of Corrosion Performance

Visual examination of the specimen surfaces in solution P (high total alkalinity and hardness, with consequent carbonate precipitation tendency) showed early light yellowish discoloration uniformly distributed over the convex indentation surface in all dimpled specimens tested. The discoloration was indicative of ongoing, but mild, corrosion there.

Symptoms were more severe in solution C (low alkalinity and hardness, with no precipitating tendency), where strong reddish discoloration was first noted early on the convex indentation of all dimpled specimens, and gradually propagating covering the entire indentation surface (Figure 4-5).

Figure 4-5. Severe Corrosion at a 1-in Convex Dimple Exposed to Solution C. (Picture shows immersed sample surface at 19 days exposure).

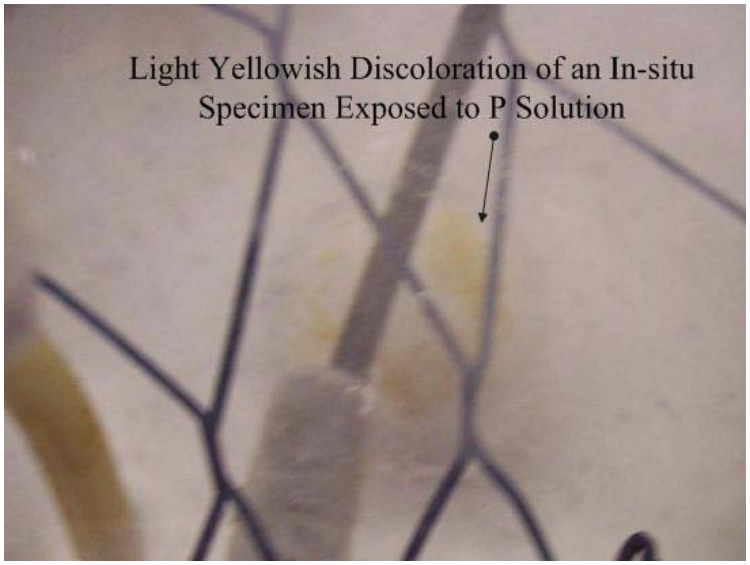

Figure 4-6. Light Corrosion at a 1-in Convex Dimple Exposed to Solution P. (Picture shows immersed sample surface at 21 days exposure).

In either solution corrosion appeared to be more intense for the 1-in diameter indentation specimens. However, it is noted that the deformed area was greatest for those specimens even though maximum local strain may have been less severe than for the smaller radius indentation specimens. In both solutions, corrosion of the flat aluminized surface around the dimple and associated deformation was minimal, suggesting preservation of passive behavior there. Correspondingly, no sign of corrosion was observed either in any of the flat surface specimens exposed to both solutions, suggesting good corrosion performance in those cases at least during the time period investigated to date. Clearly, any galvanic protection from the aluminized portion was insufficient to avoid initiation of active corrosion of the exposed steel especially in the solution C, in agreement with the results reported elsewhere for specimens with machined coating breaks (Caseres, 2007). It is noted that in the work by Caseres (Caseres 2007) activation of flat aluminized surfaces tended to take place in some circumstances after longer exposure times (e.g. 2,000 hrs or more). Future testing will examine that possibility.

4.3 E_{OC} Trends and Corrosion Behavior

The E_{OC} tended to fluctuate upon laboratory temperature changes. In order to compensate for that temperature effect to better evaluate E_{OC} trends with time, all potentials were converted to estimated values at 23 C^o. The conversion was made by first plotting the change in potential between consecutive day readings as function of the corresponding change in temperature. The data followed an approximately linear trend in that relatively narrow interval, with a trend slope of 0.0204 $V/^oC$. That result was thus approximated by:

$E(T+\Delta T) = E(T) - \Delta T.\ (0.0204)\quad V/^{o}C$ Eq(3)

$E(23\ C^{0}+\Delta T) = E(23\ ^{o}C) - (T_m-23C^{0}).\ (0.0204)\quad V/^{o}C$ Eq(4)

$E(23\ ^{o}C) = E(T_m) + (T_m-23C^{0}).\ (0.0204)\quad V/^{o}C$ Eq(5)

Where T_m is the measured temperature and $E(23^{o}C)$ is the estimated value that E_{OC} would have adopted if the test temperature was $23^{o}C$.

This correction is an empirical adjustment to assist in revealing longer time potential trends, and it is not assigned mechanistic significance at present. However, future work will assess if the corresponding activation energy that can be derived from this analysis may provide an additional descriptor of the kinetics of reactions relevant to the corrosion process.

Figure 4-7 exemplifies the average E_{OC} trends versus exposure time for the different indentation radii exposed to solution C. It is noted that in previous work (Caseres and Sagüés, 2006) with these solutions the E_{OC} of plain steel was found to be in the order of ~-600 to -700 mV, while an unblemished aluminized surface tended to develop potentials typically > 100 mV more negative. In the present experiments, a few hours after immersion the E_{OC} values were ~-650 mV for all specimens. The potentials then decayed to reach values of < ~-800 mV for the flat specimens, and for the dimpled specimens of 9/16-in and ¾-in indentation radii. The E_{OC} value for the dimpled specimens with 1-in indentation radius was ~100 mV more positive compared to all the other specimens. That observation showed that the severity of the indentation (as pointed out above, apparently responding in these tests more to the total area affected than to how strong it is locally) played an important role in dictating the overall system potential. This potential elevation likely reflected the presence of a substantial number of

microscopic aluminized coating breaks exposing the underlying steel base in the 1-in indentation specimens, which dominated the overall potential trends in those cases. The general declining trends of both flat and formed specimens, however, suggest that the potentials are approaching that of corroding aluminum as exposure time increases. In the more aggressive solution C, the aluminum coating may tend to depassivate and provide galvanic protection for steel; however, this protection if present was not sufficient during the test period examined so far to prevent the corrosion of bare steel exposed to the solution. Indeed, appreciable corrosion of steel manifested as brownish discoloration was observed in the dimpled region, which is expected to have numerous microfissures.

In solution P there was much scatter in the data but the flat samples had in average the most negative potentials compared to formed samples. There was an increasing E_{OC} trend with time for all specimens in solution P, most notably for the formed specimens, suggesting that the E_{OC} in those tended to approach the potential of corroding steel. In this benign environment the aluminum coating is likely to be in a well established passive condition, thus not providing any important galvanic protection for steel. Therefore the corrosion of unprotected exposed steel predominantly polarized the system and caused a elevating trend of potentials in the system. However, it is noted that the specimens in solution P exhibited only light discoloration at the indentation, so that the E_{OC} trend toward more positive values may be eventually arrested if the above interpretation is correct.

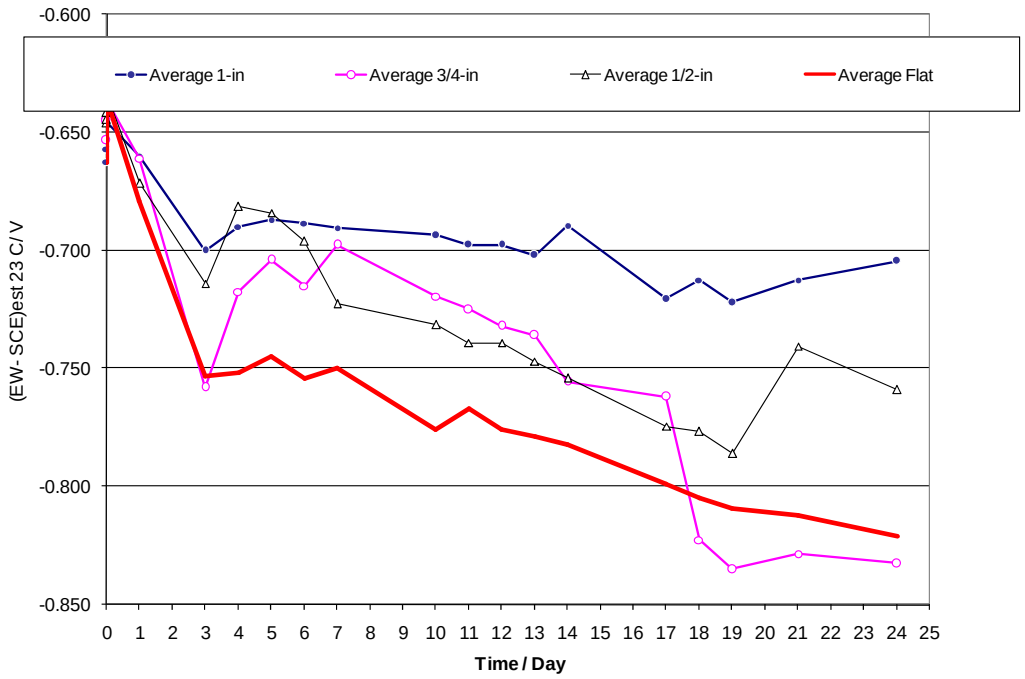

Figure 4-7. E_{OC} Trends versus Exposure Time in Solution C

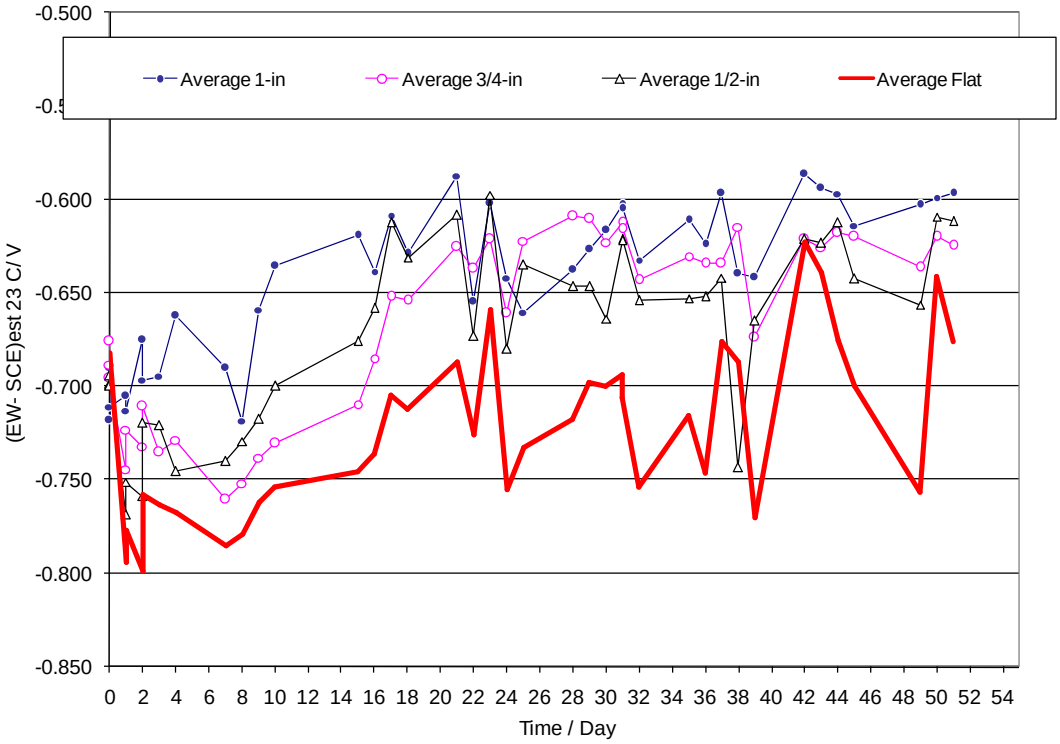

Figure 4-8. E_{OC} Trends versus Exposure Time in Solution P

4.4 Impedance Behavior

The analog circuit used to fit the EIS data is shown in Figure 4-9. This analog[1] was chosen mainly for overall simplicity and having provided a reasonable account of the observed impedance spectra. A more complicated circuit is expected to be needed for later stages of the system evolution (Caseres, 2007). Rs represents the effective solution resistance. The analog circuit consists of a polarization admittance (Rp^{-1}) reflecting the combined activation polarization of the anodic and cathodic reactions, in parallel with a Constant Phase Element (CPE) representing the interfacial charge storage at the metal surface. The proposed analog circuit yielded good best-fit simulations of the EIS responses in both solutions.

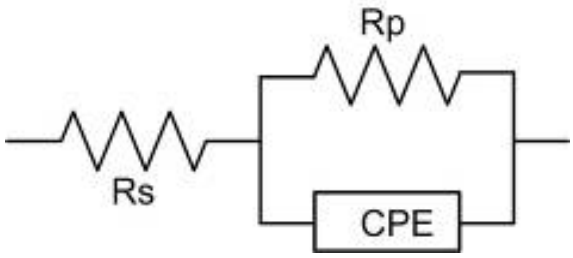

Figure 4-9. CPE Model Used to Fit the EIS Results

Figure 4-10 illustrates the EIS results of the flat and 1-in indentation specimens exposed to solution C at 4 and 10 days after exposure. The 1 mHz impedance moduli for the flat specimens showed increasing trends attaining ~11 kΩ after 10 days, consistent with generally passive behavior and the absence of visual evidence of active corrosion. In contrast, the 1 mHz impedance moduli for the 1 in indentation specimen in C were ~ < 2

[1] In general, the analog circuit chosen to represent the impedance response for the present cases may not be unique; alternative analog circuits may explain equally well the observed impedance behavior.

kΩ and roughly constant with exposure time. Comparison of results computed by fitting the data per the Figure 4-9 analog circuit for all the specimens are shown in Figure 4-12. The comparison shows that in solution C the dimpled specimens had distinctly lower Rp values (and consequently stronger indication of corrosion) than the flat specimens. These results are consistent with the visual observations and provided further evidence that forming distress, at the levels explored here, promotes corrosion of the aluminized composite in the non-scaling, more aggressive solution tested.

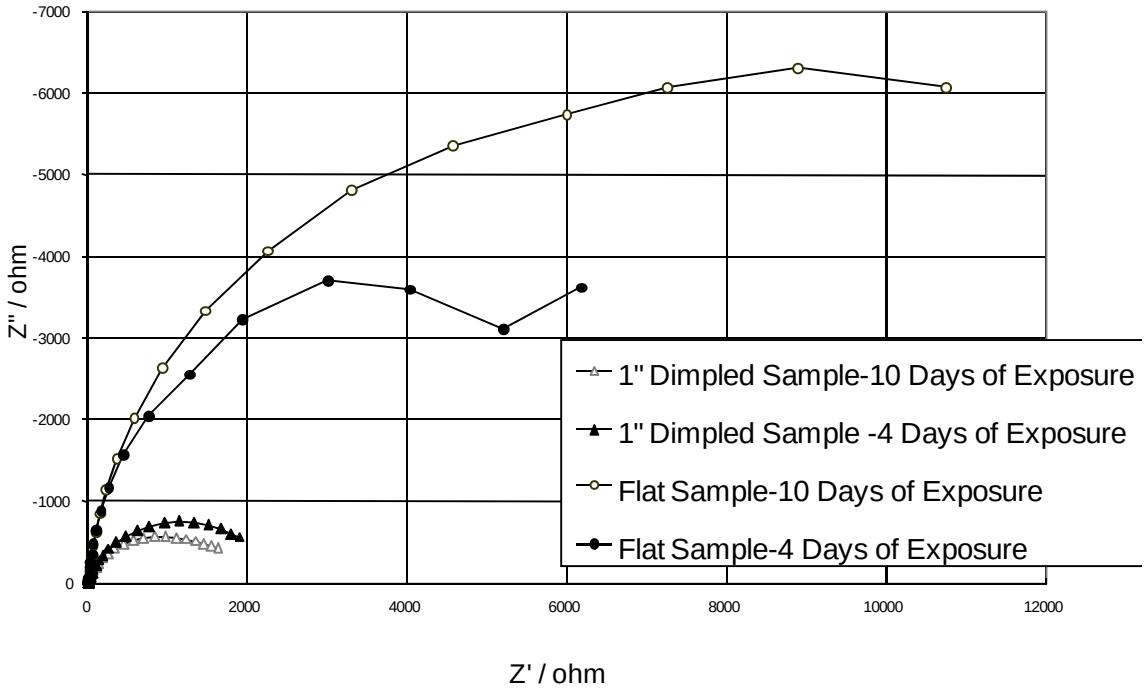

Figure 4-10. EIS Results of the Flat and 1-in Indentation Specimens Exposed to Solution C. Bode diagram is presented in Appendix B.

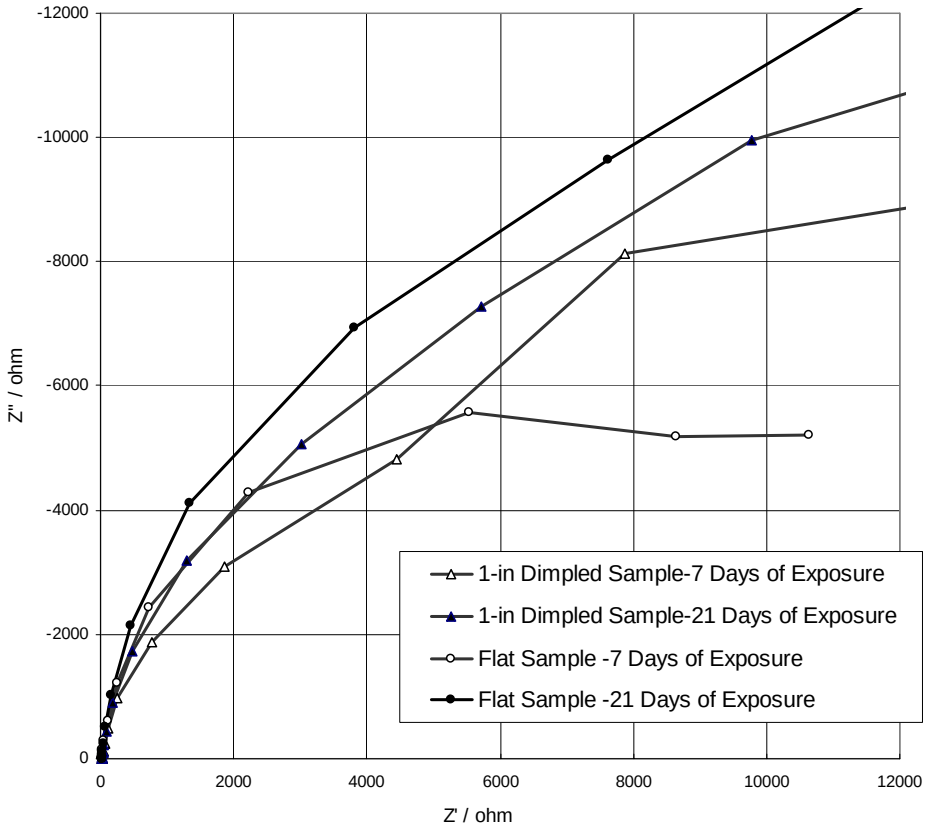

Figure 4-11. EIS Results of the Flat and 1-in Indentation Specimens Exposed to Solution P. Bode Diagram Is Presented in Appendix C.

Impedance diagrams of specimens in the more protective Solution P showed much larger low frequency impedance moduli than in Solution C, and less differentiation between flat and formed specimens.

The relative Rp values and variability for the various dimple sizes in both solutions and at two exposure times is further illustrated in Figures 4-12 and 4-13. Figures 4-14 and 4-15 show the nominal calculated corrosion currents assuming a Stern-Geary constant of 26 mV. Clearly the solution P is less aggressive overall and in it there is greater scatter and little differentiation between the flat and formed specimens. The

polarization resistance on average tended to increase with time (with matching decreasing time for the apparent corrosion current) attesting to the protective character of this precipitating solution.

In the more aggressive solution C, Rp values are about one order of magnitude lower (or I_{Corr} values one order of magnitude higher) than in the solution P, and there is notably more apparent corrosion current in the formed than in the flat specimens. There seems to be a trend of increasing Rp (decreasing I_{Corr}) with time but not consistent for all test conditions.

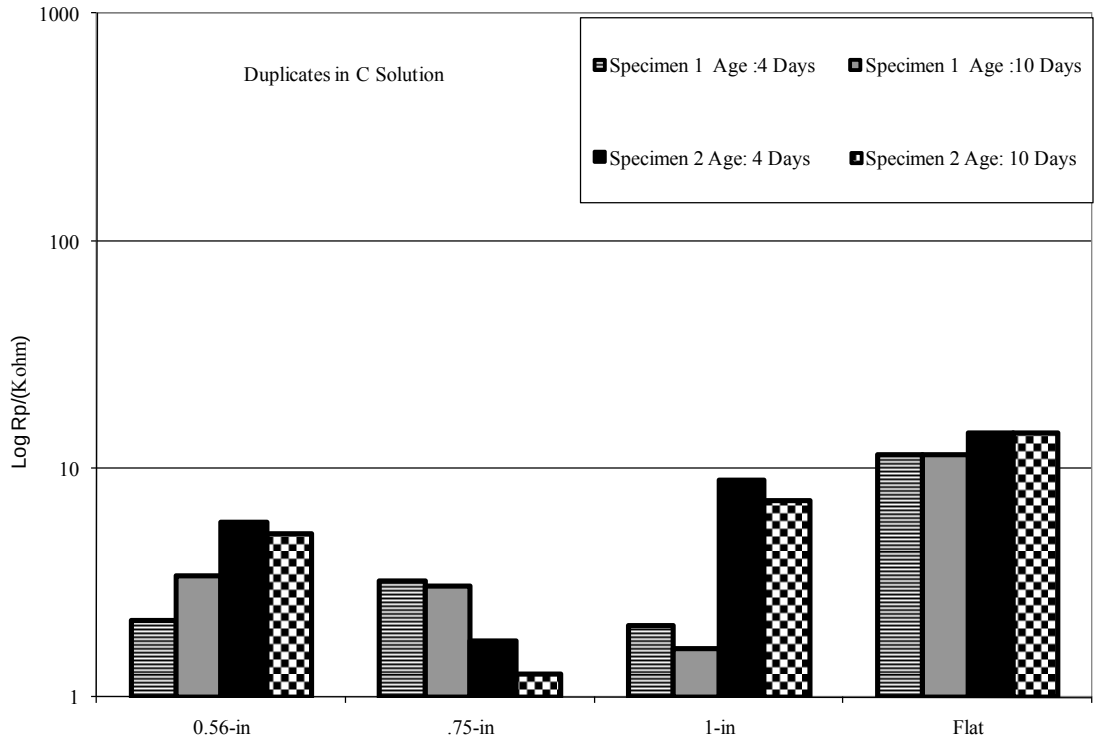

Figure 4-12. Polarization Resistance Values for Different Bent Categories at Two Exposure Times in Solution C

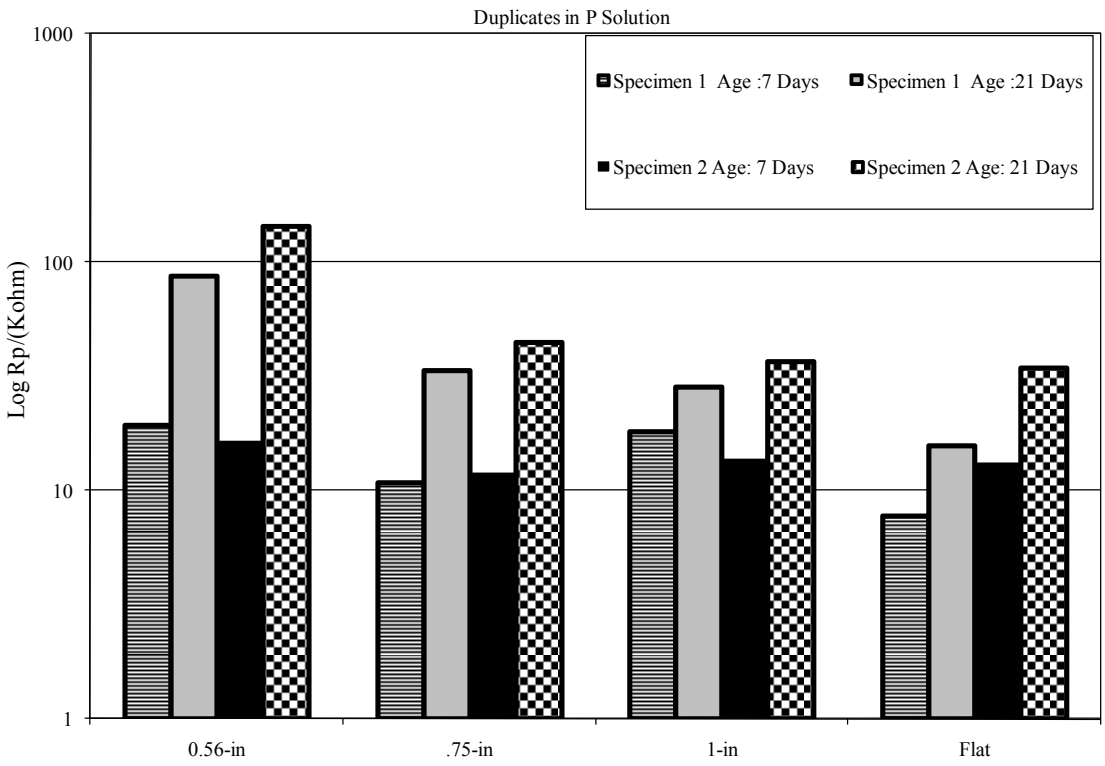

Figure 4-13. Polarization Resistance Values for Different Bent Categories at Two Exposure Times in Solution P

At this time, no clear differentiation in behavior has been established between specimens formed with different radii indentations, in part because of the early stage of the tests and also because the relative area of the mechanically distressed zones has not been quantitatively determined. Long-term monitoring of specimens, and development of ways to account for surface area normalization of corrosion at the different indentation sizes, is in progress. An initial attempt at normalization is presented next.

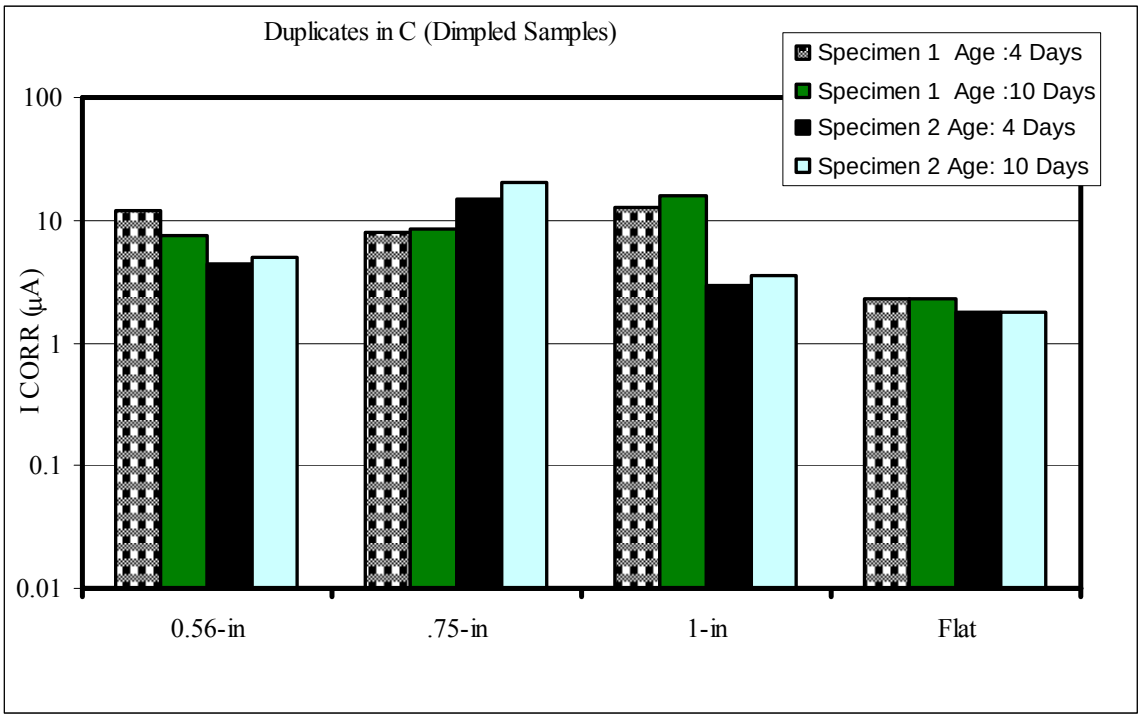

Figure 4-14. I_{Corr} Trend of Deep Drawn Specimens with Various Radii in Solution C

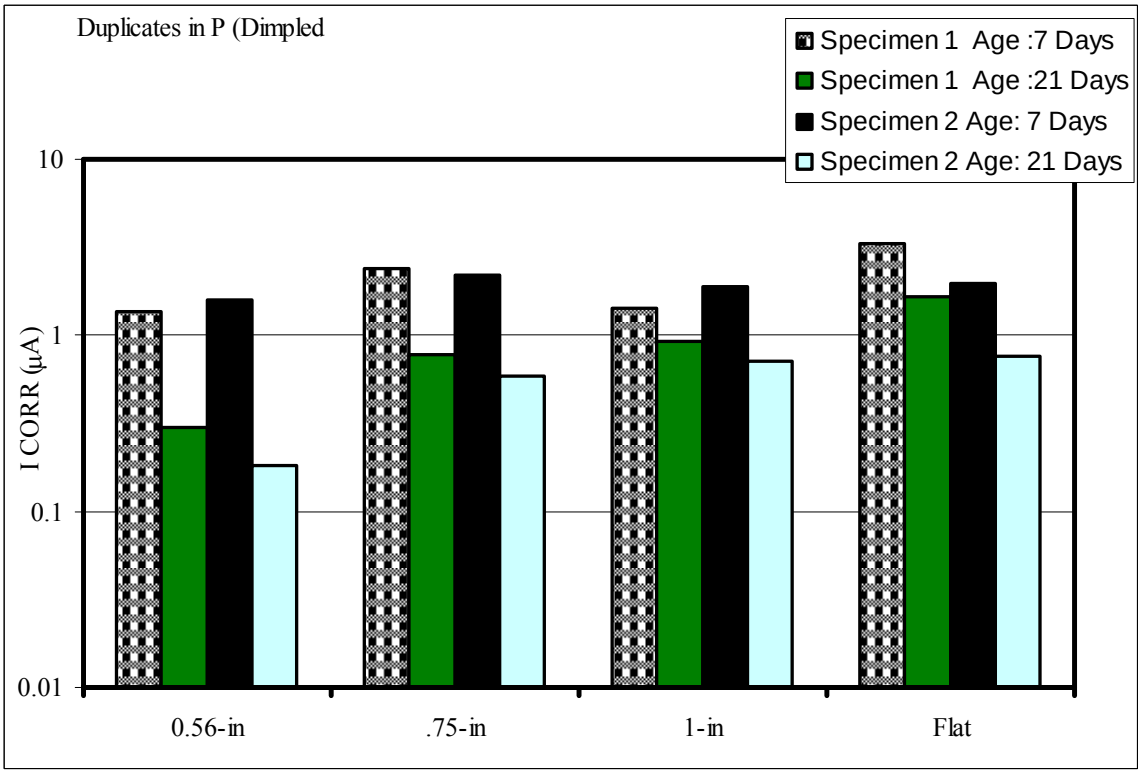

Figure 4-15. I_{Corr} Trend of Deep Drawn Specimens with Various Radii in Solution P

Although a precise evaluation of the area specific corrosion rate cannot be done at this time, on first approximation the expected corroding area can be assumed to be the same as the area of a circle with a diameter equal to the diameter of the indenting steel ball. Therefore, the corrosion current value obtained based on polarization resistance (Figures 4-14 and 4-15) can be divided by those nominal corroding areas to obtain a nominal corrosion current density i_{Corr}. In order to account for the apparent corrosion rate of the flat portion, the average corrosion current of control flat samples was first subtracted from the average corrosion current of the formed samples. The analysis was only performed for the specimens exposed to the solution C where flat-formed differentiation was apparent. The resulting nominal current density of the formed region is shown in Figure 4-16. These results show greater nominal corrosion current densities, (by about one order of magnitude) in the two lower indentation diameter cases than in the 1-in diameter case. This finding agrees with the expectation that more sharply formed material may attain a higher corrosion rate. The highest nominal corrosion current densities are in the order of a few $\mu A/cm^2$, which correspond to average metal penetration rates in the order of a few tens of micrometers per year. Such rates, if sustained over the long term could be of concern in significantly reducing the time for local perforation of a pipe wall.

4.5 Long Term Trends and Continuation Studies

This investigation has been predominantly of exploratory character and served to set the methodology and preliminary trends toward long term evaluation of the effect of forming on corrosion performance of formed aluminized steel. The experimental set ups

created in this work will undergo continuing testing over extended periods (e.g. > 3,000 hrs) to establish long term effects of forming on corrosion. Of particular interest will be to assess whether activation of the aluminum takes place later on as seen elsewhere (Caseres 2007), which could have an important protective effect on the formed regions seen to undergo early corrosion in the tests performed to date. Analysis will also be extended to better characterize the extent of mechanical damage for the dimpled geometry and that used in actual production ribbed culvert pipes.

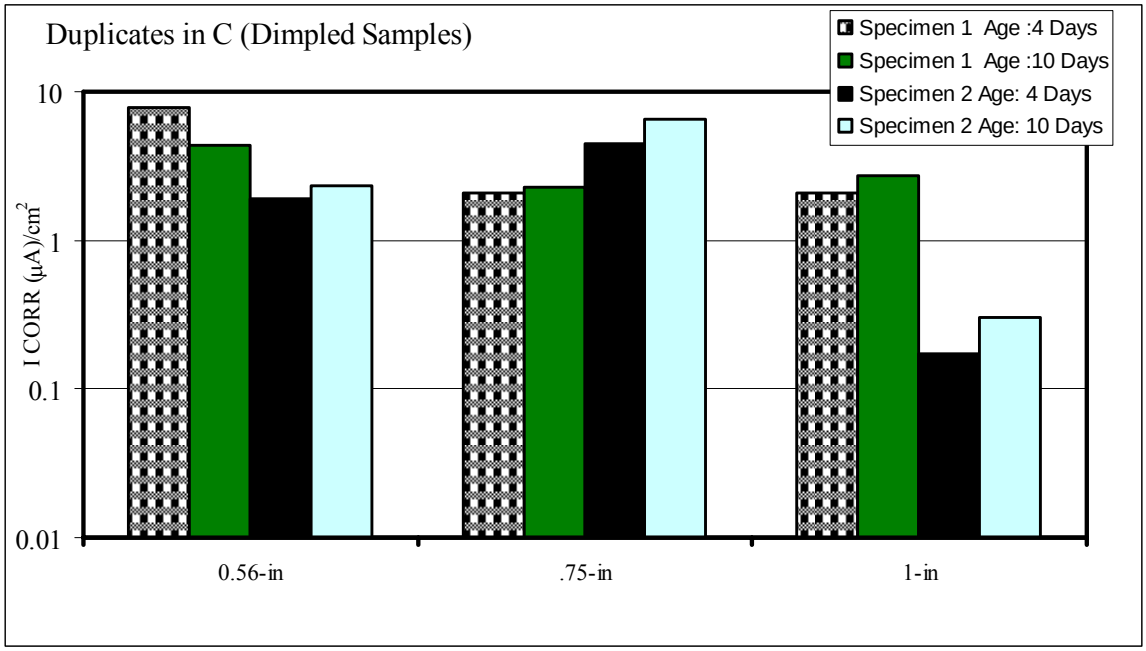

Figure 4-16. i_{Corr} (Nominal Current Density) Trend of Deep Drawn Specimens with Various Radii in Solution C

Chapter Five

Conclusions of Deep Drawn Aluminized Steel Experiments

- Forming by bending results in brittle fracture of the inner (intermetallic) aluminized coating layer, in a manner consistent with predictions of simplified bending mechanics of the system. Failure of the outer (mostly aluminum) layer by ductile deformation was much less common.

- The convex portion of specimens formed by spherical indentation was susceptible to early corrosion development in moderately aggressive simulated natural water. Not formed (flat) aluminized control surfaces showed much less deterioration during the test interval (from visual and electrochemical evidence).

- Both formed and control specimens showed little corrosion damage when exposed to a more benign, precipitating simulated natural water solution.

- Open Circuit Potentials in precipitating solutions with high precipitating tendency suggested a increasing trend in which potentials are approaching the potentials of corroding steel. In more aggressive solution with low precipitating tendency, potentials illustrated a declining trend approaching the potential of corroding aluminum.

- The above are preliminary findings from tests in progress. Confirmation as well as revealing the evolution of other modes of deterioration is pending on longer term evaluation with the test assemblies created in the present work. .

- Additional Future work will focus on analyzing the strain of deep drawn specimens, and establishing a relationship between the strain and corrosion rate of exposed specimen.

References

AK Steel, Aluminized Steel Type 2 Product Features, (2007) http://www.aksteel.com/pdf/markets_products/carbon/T2_Data_Bulletin.pdf.

Akhoondan M., Sagüés A. (2007), Corrosion of Mechanically Formed Aluminized Steel, Student Poster /2007, NACE International, Nashville, TN, 2007 (Archived 2nd Place of Herro Award for Best Student Poster).

Akhoondan M, Sagüés A., Cáseres L. (2008), Corrosion Assessment of Mechanically Formed Aluminized Steel, submitted for publication as Corrosion/2008, Paper No. (1462), NACE International, Houston, TX, 2008.

Amercian Society for Metals, 1972, 8th Ed., Vol. 7, Ohio.

Amit Kumar Gupta, D. Ravi Kumar (2006), Formability of galvanized interstitial-free steel sheets, Journal of Materials Processing Technology, 172, pp. 225-237.

An J., Liu Y.B., Sun D.R. (2001), Mechanism of Bonding of Al–Pb Alloy Strip and Hot-Dip Aluminised Steel Sheet by Hot Rolling, Materials Science Technology 17, pp. 451-454.

Armstrong R.D., Braham V.J. (1996), the Mechanism of Aluminum Corrosion in Alkaline Solutions, Corrosion Science 38, pp. 1463-1471.

Bednar L. (1989), Galvanized Steel Drainage Pipe Durability Estimation with a Modified California Chart, Paper No. 88-0341, 68th Annual Meeting, Transportation Research Board, Washington, D.C.

Caseres L. (2007), Electrochemical Behavior of Aluminized Steel Type 2 in Scale-Forming Waters, Ph.D. Dissertation, University of South Florida.

Caseres L. and Sagüés A. (2006), Galvanic Behavior of Type 2 Aluminized Steel in Simulated Natural Waters", L. Cancun, Mexico, "Corrosion of Infrastructure", The Electrochemical Society, Pennington, NJ, 2007, ECS Transactions Vol. 13, Issue 13, 210th ECS Meeting , October 29-November 3, 2006, pp. 147-157.

Caseres L., Sagüés A. (2005), Corrosion of Aluminized Steel in Scale Forming Waters, Paper No. 05348, 13 pp. Corrosion/2005, NACE International, Houston, 2005.

Castro P., Sagüés A ., Moreno E.I., Maldonado L., Genesca J. (1996), Characterization of Activated Titanium Solid Reference Electrodes for Corrosion Testing of Steel in Concrete, Corrosion 52, p. 609.

Cerlanek W.D., Powers R.G. (1993), Drainage Culvert Service Life Performance and Estimation, State of Florida Department of Transportation Report No. 93-4A.

Creus J., Mazille H., Idrissi H. (2000), Porosity Evaluation of Protective Coatings Electrodeposited on Steel, Surface and Coatings Technology 130, pp. 224-232

Dieter G., (1986), Mechanical Metallurgy, McGraw-Hill, New York, pp. 659-662.

Gul Hameed Awan, Faiz ul Hasan (University of Engineering and Technology, Lahore), (2006), The morphology of coating/substrate interface in hot-dip aluminized steels, Materials Science and Engineering, Vol. 390, pp. 437-443.

Hong, Lim, Chung, Choi (2002), Texture and Corrosion Mechanisms of Aluminized Steel Sheets, Material Science Forum, 408-412, pp. 1031-1036.

Hwang, Song, Kim (2004), Effects of carbon content of carbon steel on its dissolution into a molten aluminum alloy, Materials Science and Engineering 390, pp. 437-443.

Johnsson T., Nordhag L. (1984), Corrosion Resistance of Coatings of Aluminum, Zinc and their Alloys: Results of Four Years' Exposure, Interfinish.

Jones. D.A. (1996), Principles and Prevention of Corrosion, Prentice Hall, NJ, pp. 75-113.

Kimoto H. (1999), Corrosion Engineering 48, p. 579.

Legault R.A., Pearson V.P. (1978), Kinetics of the Atmospheric Corrosion of Aluminized Steel, Corrosion 34, pp. 344-348.

Li W., Liu S., Huang Q., Gu M. (2003), Hot- Dipped Aluminising (HDA) of a Low Carbon Steel Wire, Materials Science and Technology 19, pp. 1025-102.

Mohanty (2000), Developments in automobile steel grades-experience at TATA steel, Iron Steel Rev. Pp. 19-27.

Sagüés A. (2006), Electrochemical Impedance Spectroscopy Course Notes, University of South Florida.

Townsend H.E., Borzillo A.R. (1987), Twenty-Year Atmospheric Corrosion Tests of Hot-dip Coated Sheet Steel, Materials Performance 26, pp. 37-41.

Appendices

Appendix A: Sample Inventory

Table A-1 Number of Specimens Exposed in Each Category

Specimens	Formed Category (Indentation Size)	Solution P	Solution C
Specimens Exposed	Φ =1-in	PDIM (1) PDIM (2)	CDIM (7) CDIM (8)
	Φ =3/4-in	PDIM (3) PDIM (4)	CDIM (10) CDIM (11)
	Φ =9/16-in	PDIM (5) PDIM (6)	CDIM (13) CDIM (16)
	Flat	PF (1) PF (2)	CF(1) CF (2)

Appendix B: EIS Results from Duplicate Dimpled Specimens in Solution C

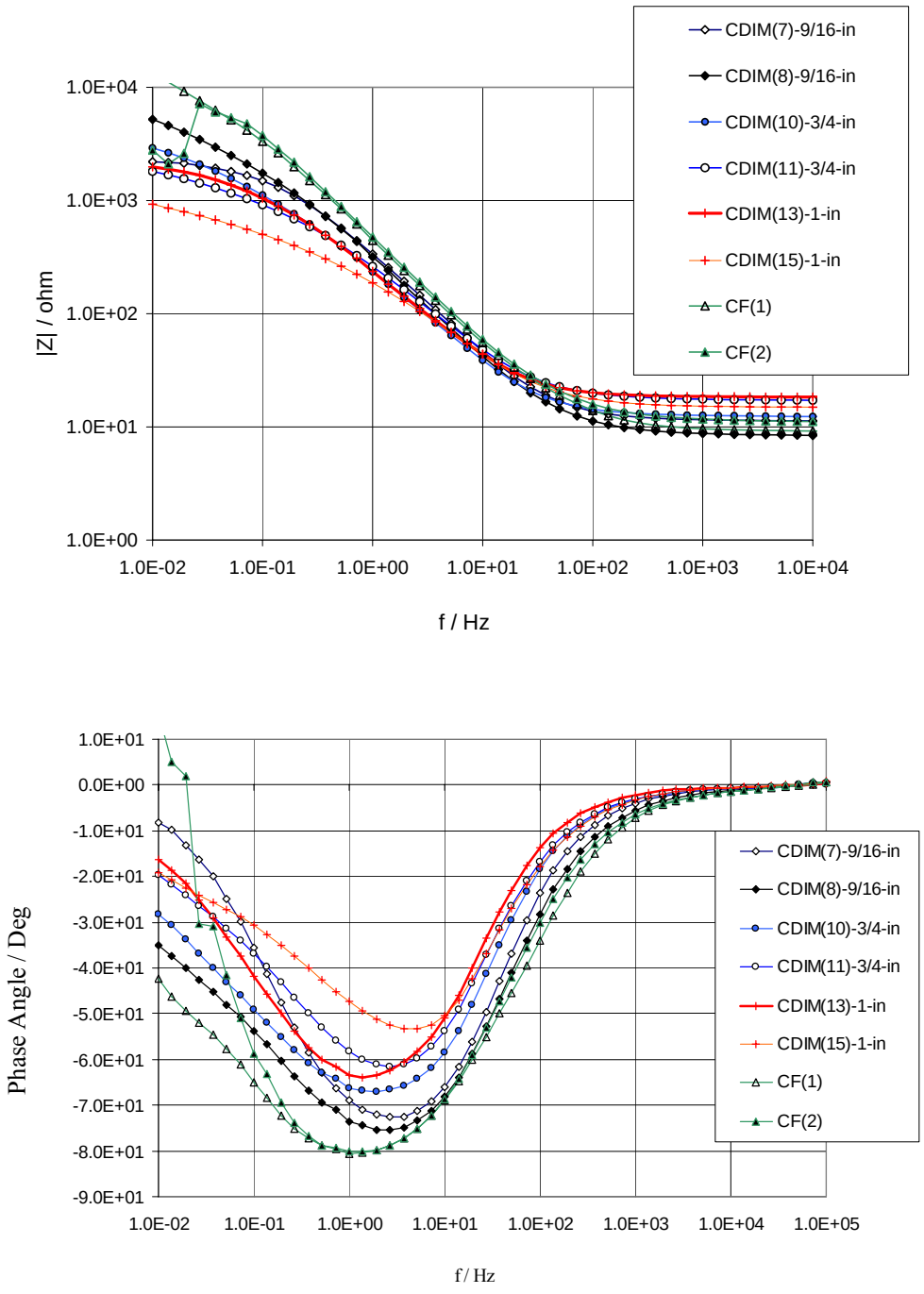

Figure B-1. EIS Results from Duplicate Dimpled Specimens in Solution C at 4 Days Bode (Top) and Phase Angle (Bottom)

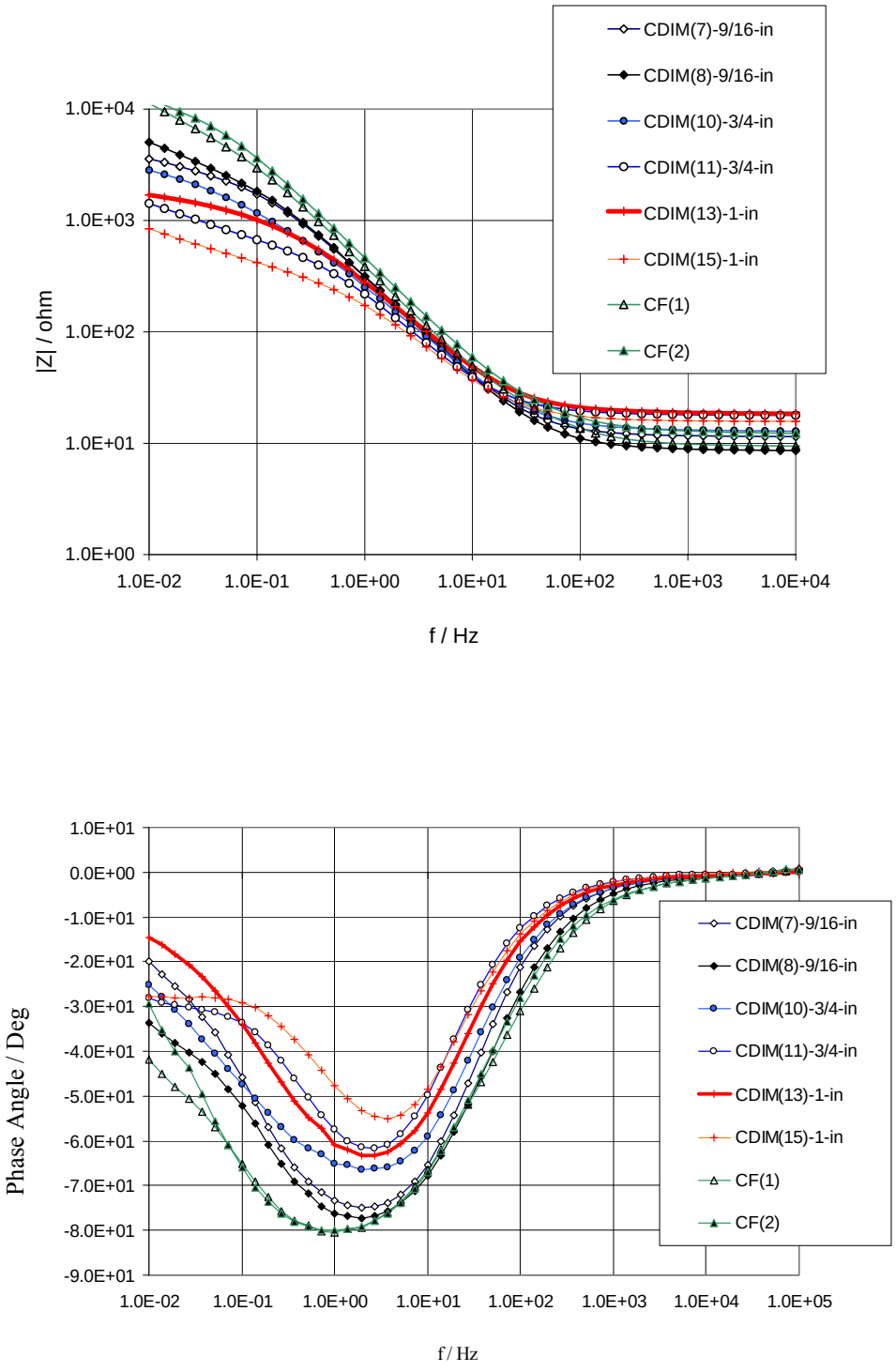

Figure B-2. EIS Results from Duplicate Dimpled Specimens in Solution C at 10-Days Bode (Top) and Phase Angle (Bottom)

Appendix C: EIS Results from Duplicate Dimpled Specimens in Solution P

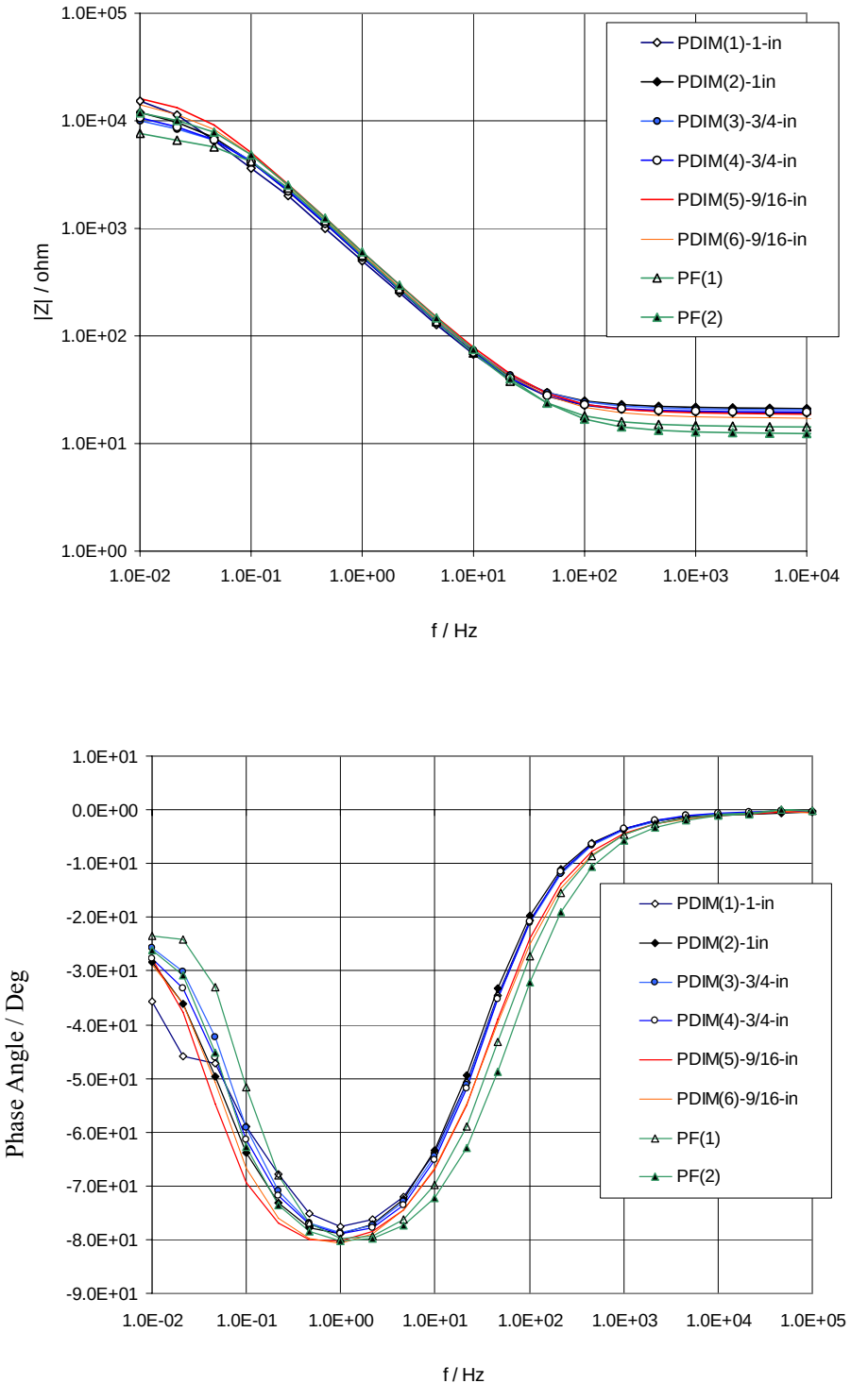

Figure C-1. EIS Results from Duplicate Dimpled Specimens in Solution P at 7-Days Bode (Top) and Phase Angle (Bottom)

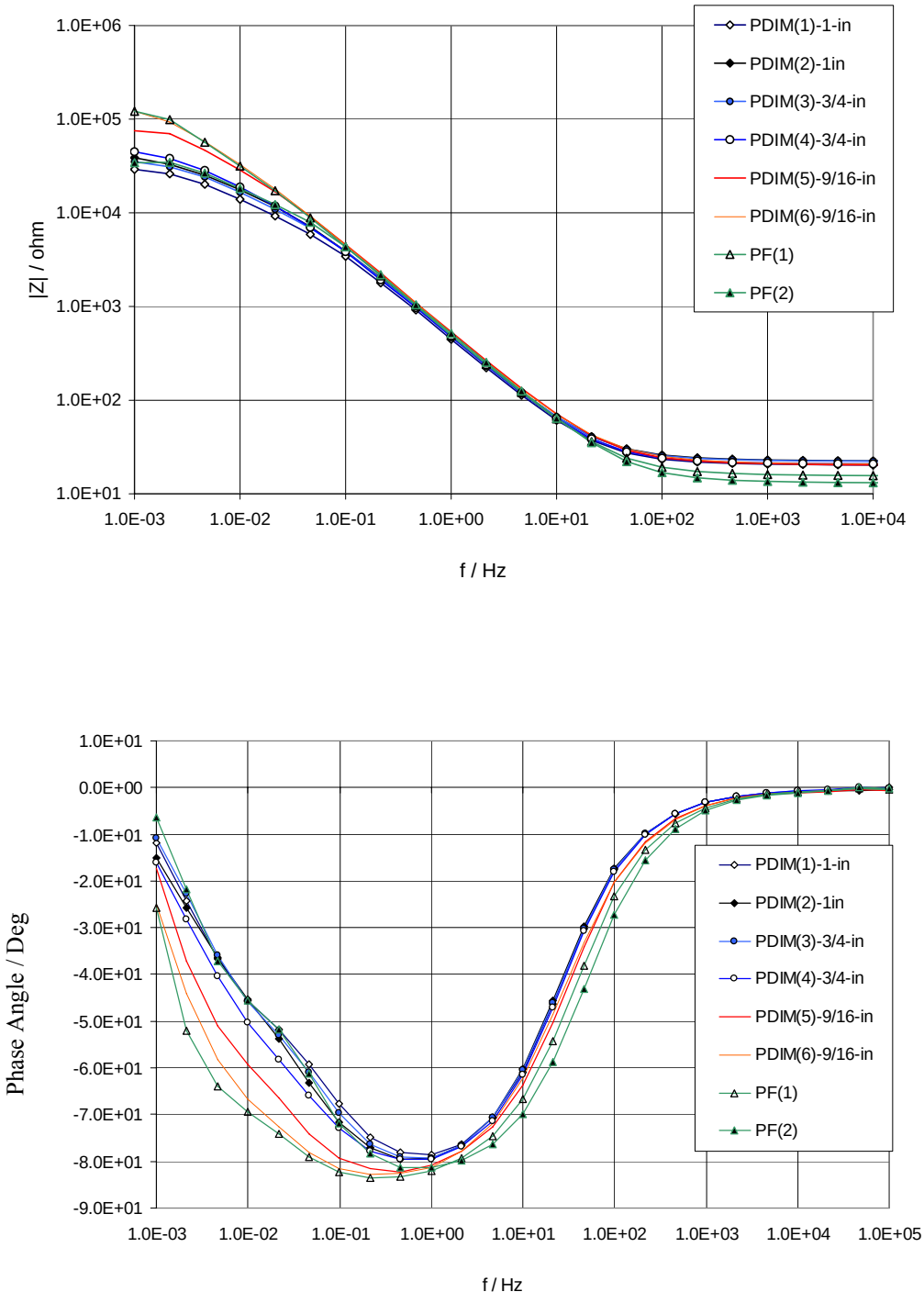

Figure C-2. EIS Results from Duplicate Dimpled Specimens in Solution P at 21-Days Bode (Top) and Phase Angle (Bottom)

Appendix D: Metallographic Examination of Dimpled Samples. (Illustration of Initial Work and Methodology Under Development).

Figure D-1. Dimpled Specimen Cut with Hack Saw

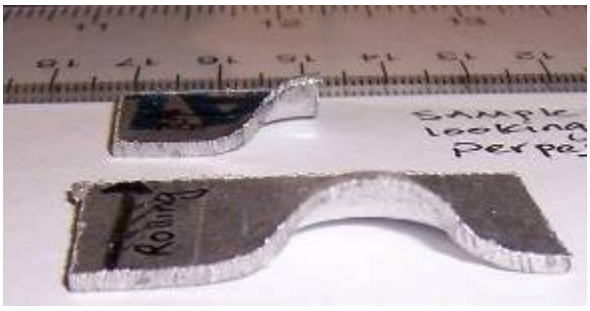

Figure D-2. Side View of Dimpled Samples Cut at Indentation Region Perpendicular to Metal Rolling Direction

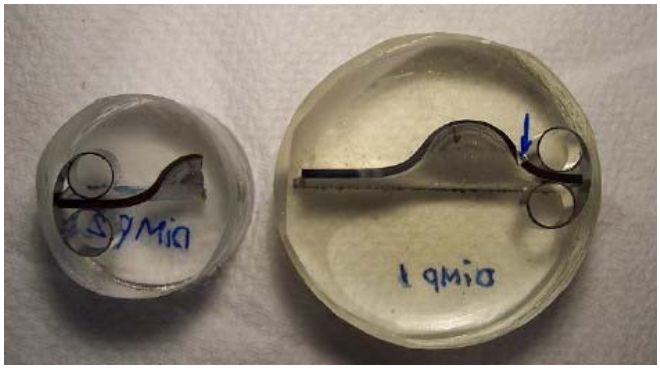

Figure D-3. Metallographic Dimpled Samples

Appendix D (Continued)

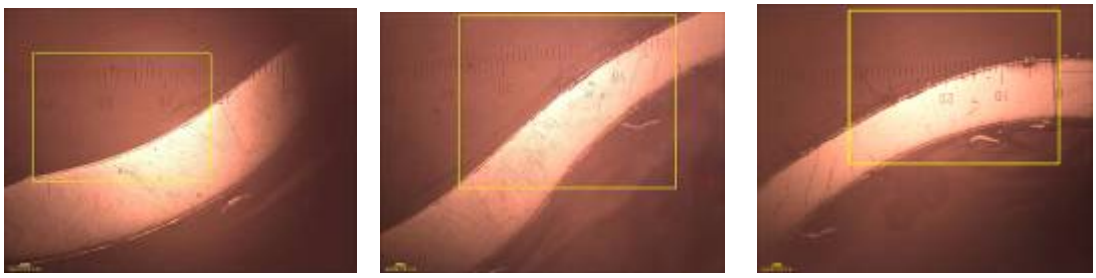

Figure D-4 Low Magnification Microscopic Photos of a Dimpled Specimen. (As It Is Seen in These Photos, the Thickness of Metal Sheet Changes Strongly Due to the Severity of the Bending Stress; Therefore, the Location of Neutral Axis Is Markedly Displaced from the Center of the Sheet).

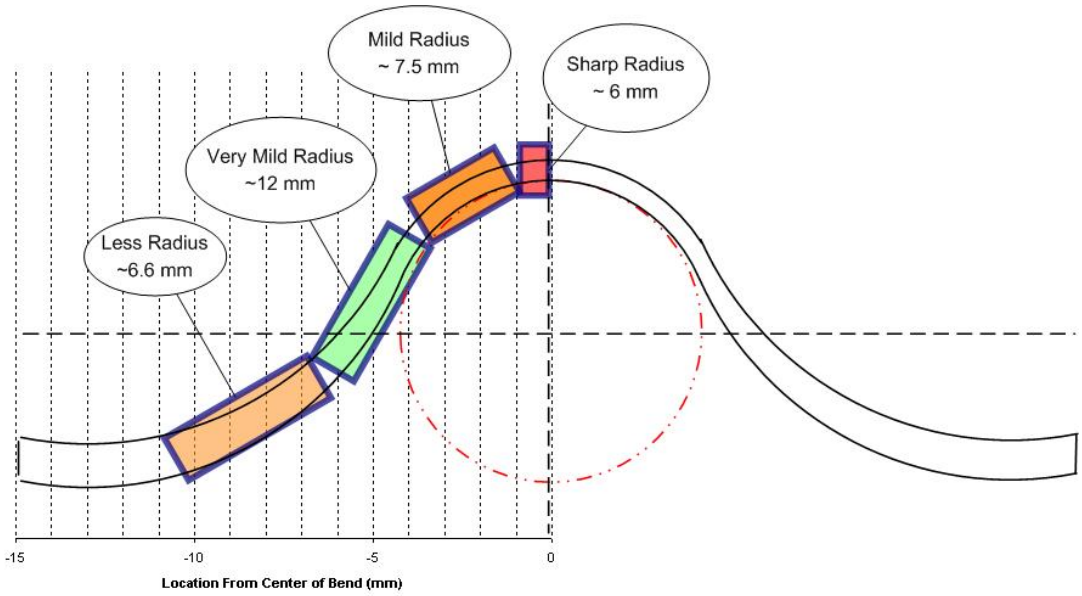

Figure D-5. Radius Mapping of 9/16-in Dimpled Sample

Appendix D (Continued)

Following illustrates the initial metallographic examination of unexposed and exposed (trial test, solution P, >500 hrs) dimpled specimens.

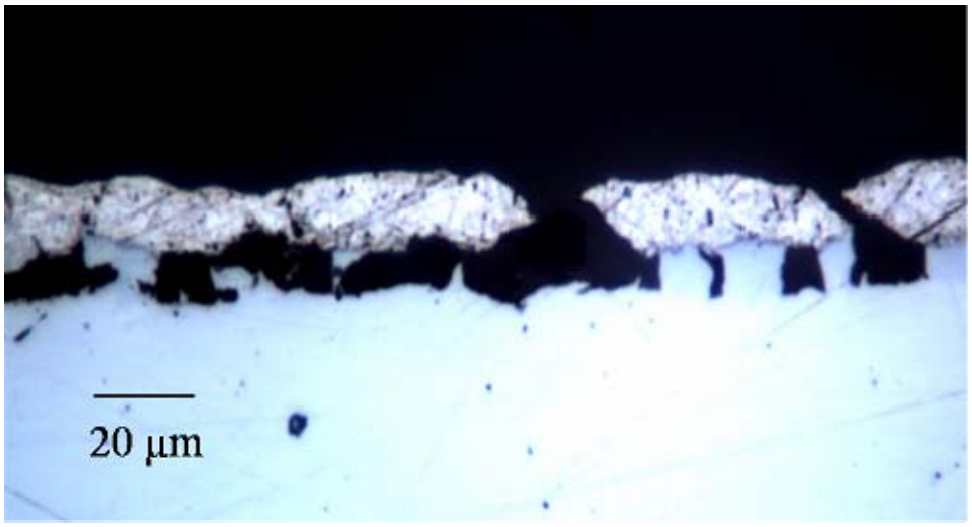

Figure D-6. High Magnification Microscopic Photo of 9/16-in Dimpled Cell Before Exposure at Indentation Region

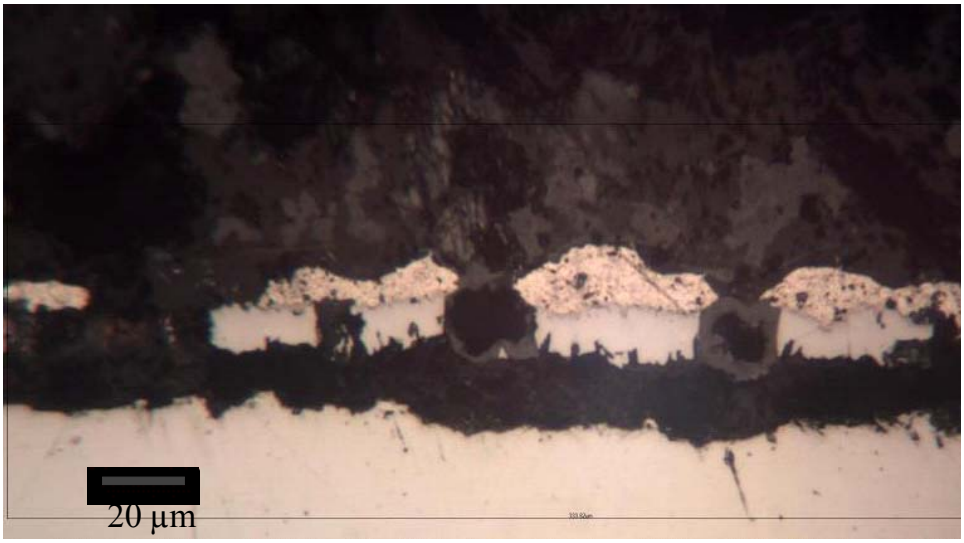

Figure D-7. Metallograph of Corroded 9/16-in Dimpled Cell at Indentation Region. (The Disappearance of Intermetallic Layer in Several Regions is Observed. This Disappearance Can Be Explained by the Corrosion of Intermetallic Layer and the Base Steel). This Issue Will Be Examined in Continuation Work).